Tectonophysics 868 (2023) 230075

Contents lists available at ScienceDirect

Tectonophysics

journal homepage: www.elsevier.com/locate/tecto

Slip localization on multiple fault splays accommodating distributed deformation across normal fault complexities

F. Iezzi [a,*], M. Francescone [b], A. Pizzi [b], A. Blumetti [c], P. Boncio [b,e], P. Di Manna [c], B. Pace [b,e], T. Piacentini [b,d], F. Papasodaro [c], F. Morelli [b], M. Caciagli [d], M. Chiappini [d], F. D'Ajello Caracciolo [d], V. Materni [d], I. Nicolosi [d], V. Sapia [d], S. Urbini [d]

[a] Dipartimento di Scienze della Terra, dell'Ambiente e delle Risorse, University "Federico II" of Naples, Italy
[b] Dipartimento di Ingegneria e Geologia, University "G. D'Annunzio" of Chieti-Pescara, Italy
[c] Istituto Superiore per la Protezione e la Ricerca Ambientale, Rome, Italy
[d] Istituto Nazionale di Geofisica e Vulcanologia, Rome, Italy
[e] UdA-TechLab, Research Center, University "G. d'Annunzio" of Chieti-Pescara, 66100 Chieti, Italy

ARTICLE INFO

Keywords:
Structural geology
Active faults
Paleoseismology
Distributed faulting
Seismic hazard

ABSTRACT

Deformation across structural complexities such as along-strike fault bends may be accommodated by distributed faulting, with multiple fault splays working to transfer the deformation between two principal fault segments. In these contexts, an unsolved question is whether fault activity is equally distributed through time, with multiple fault splays recording the same earthquakes, or it is instead localized in time and space across the distributed faults, with earthquakes being clustered on specific fault splays. To answer this question, we studied the distributed deformation across a structural complexity of the Mt. Marine fault (Central Apennines, Italy), where multiple fault splays accommodate the deformation throughout the change in strike of the fault. Our multidisciplinary (remote sensing analysis, geomorphological-geological mapping, geophysical and paleoseismological surveys) study identified five principal synthetic and antithetic fault splays arranged over an across-strike distance of 500 m, all of which showing evidence of multiple surface-rupturing events during the Late Pleistocene-Holocene. The fault splays exhibit different and variable activity rates, suggesting that fault activity is localized on specific fault splays through space and time. Nonetheless, our results suggest that multiple fault splays can rupture simultaneously during large earthquakes. Our findings have strong implications on fault-based seismic hazard assessments, as they imply that data collected on one splay may not be representative of the behaviour of the entire fault. This can potentially bias seismic hazard calculations.

1. Introduction

The geometry and dynamics of active faults are key information for seismic hazard assessments. In fact, features such as fault geometry and slip-rates are key inputs to assess the seismic hazard imposed by either ground motion or fault displacement (e.g., Coppersmith and Youngs, 2000; Youngs et al., 2003; Pace et al., 2016). However, the intrinsic nature of faulting could lead to a variety of structural arrangements of active faults, especially across complexities in the geology of faults, such as relay zones and along-strike fault bends. Analogue models and natural examples have shown that linkage of two previously isolated fault segments is driven by the development of a set of breaching faults, arranged both along and across the strike of the main faults, within their relay zone (soft-linked fault); the growth and linkage of these breaching faults will eventually allow the hard linkage of the two main fault segments, with the development of an along-strike fault bend (e.g., McLeod et al., 2000; Mansfield and Cartwright, 2001; Walsh et al., 2003). These existing models do not describe in detail how the growth and development of the multiple breaching faults proceed, and therefore we do not know whether these faults are all active at the same time.

Some information may be gained by past earthquakes. Large historical earthquakes have shown that multiple fault splays can rupture simultaneously, leading to complex patterns of coseismic slip partitioning (for normal faults see e.g., Crone et al., 1987; Beanland et al., 1989; DePolo et al., 1991; Caskey et al., 1996; Suter, 2015; see also Sarmiento et al. (2021) and Nurminen et al. (2022) for global databases

* Corresponding author.
E-mail address: francesco.iezzi@unina.it (F. Iezzi).

https://doi.org/10.1016/j.tecto.2023.230075
Received 5 June 2023; Received in revised form 15 September 2023; Accepted 12 October 2023
Available online 30 October 2023

of surface ruptures, and references therein). Small earthquake ruptures on a larger fault system may instead produce localized slip on specific sections or splays of the system (e.g., Livio et al., 2016; Civico et al., 2018; Villani et al., 2018). In addition to that, field observations have shown that coseismic slip partitioning could depend on whether surface ruptures propagate across bedrock or quaternary deposits. It has been noted that surface ruptures tend to be more distributed when propagating across loose sediments, compared to bedrock faults (e.g., 1954 M_w 6.8 Dixie Valley, Caskey et al., 1996; 1992 M_w 7.3 Landers, Milliner et al., 2015; 2010 M_w 7.2 El-Major-Cucapah, Teran et al., 2015). Hence, multiple potential scenarios of the distribution of surface ruptures can be envisaged during earthquakes, mostly due to the structural arrangement of the active fault rupturing the surface.

Understanding the role those structural complexities along active faults play in partitioning the coseismic slip provides us insights for improving seismic hazard assessments. In fact, fault-based probabilistic approaches of both ground motion and fault displacement hazard assessments rely on fault slip-rates to estimate the probability of occurrence of the next event (e.g., Coppersmith and Schwartz, 2000; Youngs et al., 2003; Pace et al., 2016; Valentini et al., 2017, Visini et al., 2020; Testa et al., 2021). Whether the coseismic slip is equally partitioned across multiple fault splays associated with a structural complexity, or it is instead localized on specific fault splays, this will strongly affect measurements of fault slip rates used for hazard assessments. If the simultaneous rupture of multiple splays across an along-strike fault bend is a recurrent pattern, then data collected on one splay may be representative of the behaviour of the entire fault. If surface ruptures are localized on one specific splay, this would record more earthquakes than the other splays. This scenario will bias following seismic hazard assessments.

In order to understand the dynamics across structural complexities characterized by distributed faulting, we focused on the Mt. Marine fault, a NW-SE, SW-dipping normal fault belonging to the Central Apennines fault system (Italy; Fig. 1). Although its fault trace is mostly localized on a bedrock fault plane, towards its SE tip the fault presents an overall change in strike accommodated by multiple fault splays arranged both along and across the strike of the main fault propagating across looser sediments (i.e. alluvial fan deposits) (Blumetti, 1995; Moro et al., 2002, 2016; Galli et al., 2011; Fig. 2). This zone of distributed faulting acts as a linkage zone of two main fault segments, the Pizzoli and Arischia segments (Fig. 2b). Previous paleoseismological surveys have studied the seismic history of some splays belonging to the Mt. Marine fault (Moro et al., 2002, 2016, Galli et al., 2011; Fig. 2a). However, these represent isolated spots within a complex system of fault splays, and therefore they do not provide a compelling picture of how the slip is partitioned across them. In addition, the distributed deformation is located within an urbanized area, which means that most of the morphological evidence of faulting has been altered, if not erased, by

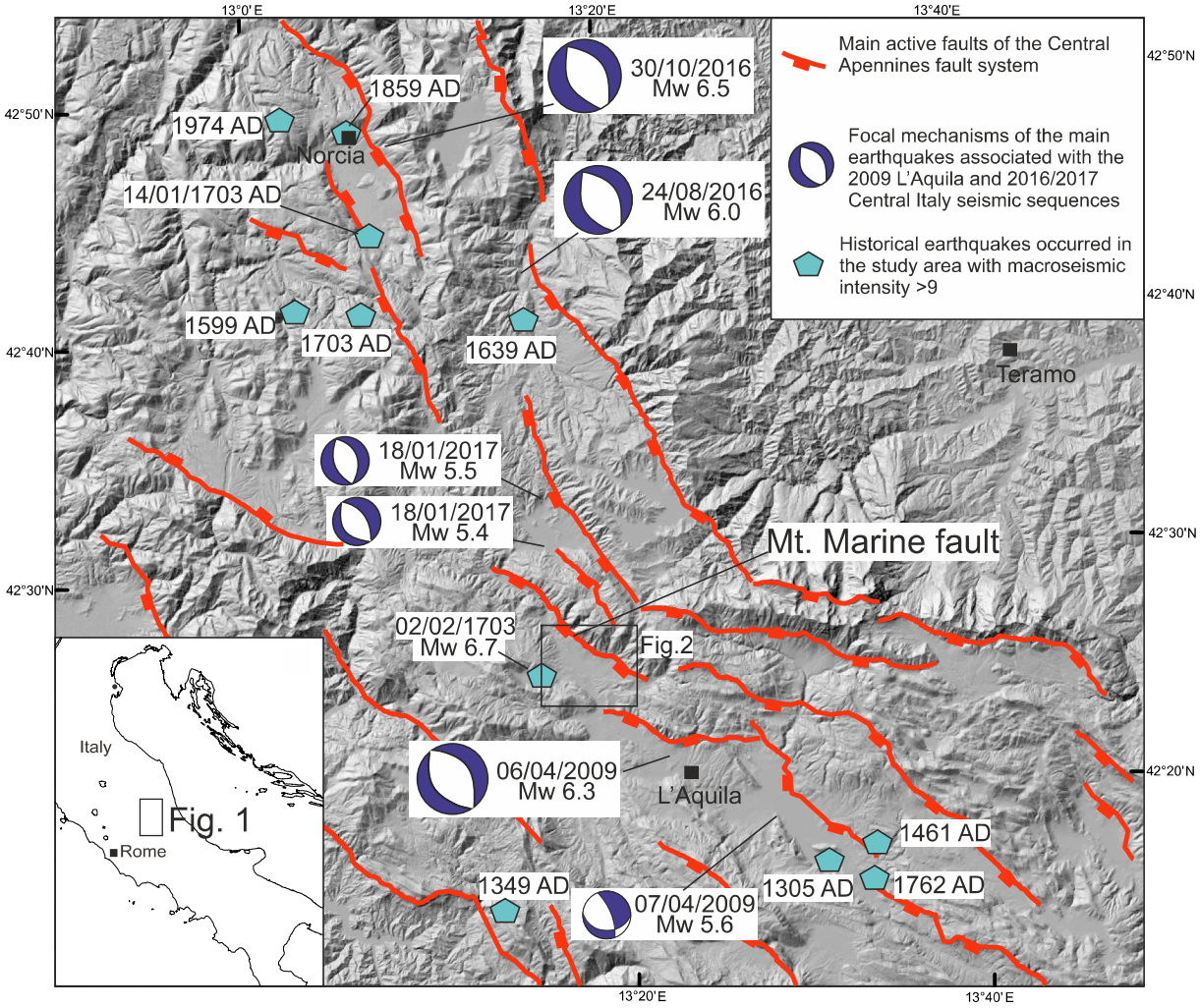

Fig. 1. Location map of the study area. In red are the main active normal faults of the Central Apennines Fault System. Pale blue polygons are epicentres of historical earthquakes (from CPTI15; Rovida et al., 2022). Focal mechanisms refer to the 2009 L'Aquila and 2016 Central Italy seismic sequences. The rectangle highlights the study area. (For interpretation of the references to colour in this figure legend, the reader is referred to the web version of this article.)

anthropic activity. The town of Pizzoli lies just above the multiple fault splays belonging to the Mt. Marine fault, with severe consequences in terms of fault displacement hazard if the fault ruptures. Within the framework of a study for the assessment of the fault displacement hazard associated with the Mt. Marine fault for the town of Pizzoli, we performed a thorough geological, geomorphological, structural, geophysical and paleoseismological study of the multiple fault splays, to reconstruct their surface trace and to define their rates of activity. We present results obtained through two paleoseismological surveys aimed at intercepting most of the fault splays characterizing the southern sector of the Mt. Marine fault (Fig. 2). We investigate the activity of these fault splays, and we discuss the implication of our findings in terms of active fault dynamics and seismic hazard assessments.

2. Geological background

The Central Apennines are a Miocene-Pliocene fold-and-thrust belt caused by the convergence of the European and African tectonic plates, which thrusted Meso-Cenozoic limestones onto Miocene flysch deposits with NE-SW shortening direction (Anderson and Jackson, 1987; Doglioni, 1991). Since 2–3 Ma, SW-NE oriented extension caused the onset of a normal fault system that dissected the previously formed thrust belt, generating large intermontane tectonic basins (Lavecchia et al., 1994; Cavinato and Celles, 1999; Piacentini and Miccadei, 2014; Cosentino et al., 2017). The normal faults strike overall NW-SE, have lengths of about 20–40 km, and generally form an array of dip-slip faults showing both en-echelon and end-on arrangements along strike (Pizzi and Scisciani, 2000; Boncio et al., 2004; Roberts and Michetti, 2004; Pizzi and Galadini, 2009; Fig. 1). These faults have the potential to generate earthquakes of medium-large magnitude (6.5–7.0) with recurrence interval of hundreds-to-thousands of years, as shown by historical seismicity recorded since Roman times (Catalogo Parametrico dei Terremoti Italiani, CPTI15; Fig. 1; Rovida et al., 2020, 2022), and paleoseismological investigations (e.g., Galli et al., 2008; Cinti et al., 2021). The horizontal extension accommodated across the Central Apennines is up to 3 mm/yr, a value matched by calculations of the extension rates using both fault slip data (Faure Walker et al., 2010, 2012) and geodetic measurements (D'Agostino et al., 2012; D'Agostino, 2014; Devoti et al., 2017).

The Mt. Marine fault is a NW-SE striking, SW-dipping, about 15 km-long normal fault located in the northern part of the Aterno Valley Fault System (Blumetti and Guerrieri, 2007; Galli et al., 2011; Iezzi et al., 2019). From a seismological point of view, the Mt. Marine fault is located between the epicentral regions of the 2009 Mw 6.3 L'Aquila earthquake and the 2016–2017 Mw max 6.5 Central Italy seismic sequence, and it lies within the epicentral area of the 2nd February 1703 Mw 6.7 historical earthquake (Fig. 1). The activity of the fault caused the formation of a hanging wall basin, infilled by hundreds of meters of Quaternary continental deposits, and a footwall limestone ridge bounded by the fault in its SW flank (e.g., Messina et al., 2001; Bosi et al., 2003; Blumetti and Guerrieri, 2007; Fig. 2). Multiple studies have explored the recent activity of the Mt. Marine fault by means of paleoseismological studies and estimations of Late Pleistocene-Holocene slip-rates obtained through measurements of the displacement of sediments and landforms (Blumetti, 1995; Galadini and Galli, 2000; Moro et al., 2002; Roberts and Michetti, 2004; Papanikolaou et al., 2005; Galli et al., 2011; Moro et al., 2016; Iezzi et al., 2019; Fig. 2). These studies have highlighted the occurrence of several surface-rupturing paleoearthquakes on multiple fault splays belonging to the Mt. Marine fault, which slips at an average rate of 0.5–0.7 mm/yr. However, none of these studies have analysed how the deformation is distributed in time and space across this narrow set of fault splays accommodating normal fault complexities.

3. Methods

We performed an integrated morphostructural study of the Mt. Marine fault, starting with multi-temporal photogeological interpretation (aerial photographs at 1:55.000 to 1:5.000 scale taken in 1945, 1954, 1981, 1985, 2004 and 2007 and made available by the Istituto Geografico Militare of Italy and Abruzzo Region, details in Supplementary Material S1), 1 m-resolution LiDAR Digital Terrain Model (DTM) analysis, made available by the Civil Protection of the Friuli-Venezia Giulia Region in 2009 (details in the Supplementary Material S1). This was followed by geological-geomorphological fieldwork (at a $>$ 1:5.000 scale), which aimed at defining the geometry of the fault system and at verifying the nature of potential fault scarps identified by the remote sensing analysis. The fieldwork was based on the mapping of the geological and tectonic features of the bedrock, the quaternary continental deposits affected by the faults, and the landforms in the fault zone (e.g., tectonic and structural, gravity-induced, fluvial and anthropogenic landforms). These activities allowed us to identify two suitable sites for investigating distributed faulting: the Vallicella site, which intercepts the upper fault splays (Figs. 2, 3, 4 and 5), and the Collemusino site, which intercepts the lowermost fault splays (Figs. 2, 6 and 7).

The morphostructural study highlighted the presence of multiple potential fault scarps. However, most of the scarps have been severely altered by anthropic activity, and therefore there may be some questioning on the tectonic nature of some of them. To verify the nature of such scarps, and whether there could be other fault splays lacking a surficial expression, we performed an integrated geophysical survey composed of Electrical Resistivity Tomography (ERT) and Ground Penetrating Radar (GPR) (Figs. 3a, b and 6a, b).

ERT profiles were acquired to investigate the subsurface units based on their electrical properties. A series of 2D vertical sections, indicating electrical resistivity values, represents the final product and layout of the data acquisition and modelling steps. Using a SYSCAL-Pro switch resistivity meter (IRIS Instruments), we acquired 3 profiles configured with 32–48 electrodes spaced 2–5 m apart. The instrument was configured to inject a square wave signal for 250 ms; both dipole-dipole and Wenner array configurations were applied, aimed at obtaining good vertical and horizontal resolution of the subsurface resistivity contrasts (Loke, 2012). An appropriate electrical coupling between adjacent electrodes and soil was achieved by recording a resistivity ground contact of about 1 kΩ. The exact location of the electrodes was achieved using a differential GPS unit that guaranteed a spatial error of $<$5 cm. To obtain true resistivity values from the measured apparent resistivity data, we used the smoothness-constrained least squares method considering models with an infinite perpendicular extension along the profile strike (Constable et al., 1987; DeGroot-Headlin and Constable, 1990; Morelli and Labrecque, 1996). The 2D ERT inversion models are based on the joint inversion of apparent resistivity data acquired on the ground surface using dipole-dipole and Wenner arrays. We conducted a 2D inversion using the software "Tomolab" (http://www.geostudiastier.it). The inversion algorithm required a target RMS error, which was determined using the root mean squared (RMS) error method and set at 1%. The inversion model space is divided into cells, with each cell defining a finite region with constant resistivity. The horizontal and vertical dimensions of these cells in the inversion region were set to half of the mean distance between electrodes, which equates to 1 m and 2.5 m for the ERT profiles with electrode spacings of 2 m and 5 m, respectively. The inversion procedure followed entails conducting the minimum number of iterations necessary to achieve the required RMS error, accepting the model once the absolute error stabilizes, and ensuring that the smoothness coefficient remains within an acceptable range, as defined by the Tomolab software's specifications. Inversion results are shown in Figs. 3b, 6b and Fig. S3 in Supplementary Materials.

The GPR surveys were carried out overlaying the ERT profiles using a GSSI Sir 4000 instrument equipped with a 200 MHz digital antenna. The investigation range was 200 ns, with a scan sampling of 512, while the

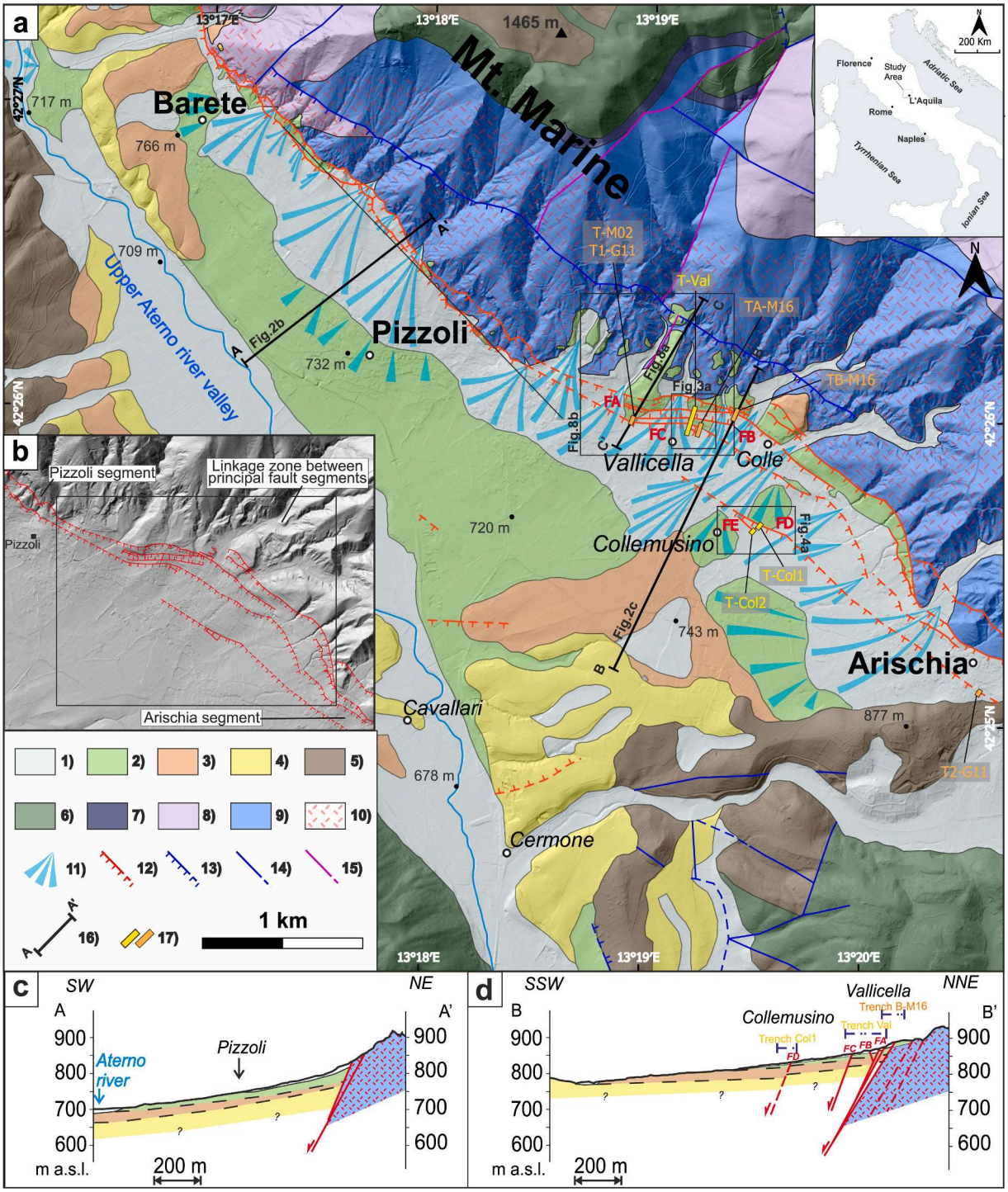

Fig. 2. Map of the Mt. Marine fault. A) Geological map of the Mt. Marine fault, modified from CARG geological sheet "348 Antrodoco" (Servizio Geologico d'Italia, 2022). The map highlights how the fault changes the structural arrangement in its southern part, where multiple splays accommodate an overall strike variation. The rectangles highlight the location maps of Vallicella site (Figs. 3a and 8) and Collemusino site (Fig. 6a). Legend: Quaternary continental deposits - 1) Holocene alluvial plain, alluvial fan and eluvial-colluvial deposits. 2) Late Pleistocene alluvial fan, slope and eluvial-colluvial deposits. 3) Middle Pleistocene alluvial fan and eluvial-colluvial deposits. 4) Early Pleistocene alluvial fan, slope and lacustrine deposits. Bedrock - 5) Paleocene-Miocene marls and calcareous marls of slope to carbonate ramp facies. 6) Upper Jurassic - Cretaceous limestones of slope to basin facies. 7) Jurassic limestones and marly limestones of condensed basin facies. 8) Jurassic limestones of slope to basinal sequence facies. 9) Lower Jurassic dolostones and dolomitized limestones of inner carbonate platform facies. Other symbols - 10) Cataclastic belt on bedrock. 11) Alluvial fan. 12) Active and capable normal fault (dashed when uncertain). 13) Normal fault on bedrock (dashed when uncertain). 14) Fault on bedrock (dashed when uncertain). 15) Jurassic sinsedimentary fault (dashed when uncertain). 16) Trace of geological cross-section. 17) Paleo-seismological trench (in yellow trenches in this study, in orange trenches from Moro et al., 2002, 2016; Galli et al., 2016). B) Fault map showing the linkage zone between the main Pizzoli and Arischia segments. C) A-A' geological cross section (Location in fig. a). D) B-B′ geological cross section (Location in fig. a). (For interpretation of the references to colour in this figure legend, the reader is referred to the web version of this article.)

Table 1
Summary table of the ^{14}C ages of samples collected in the paleoseismological trenches. The locations of samples are shown in Figs. 4, 5 and 7. The ages have been calibrated with INTCAL20 (Reimer et al., 2020).

Code Sample	Trench	Material	Method-Laboratory	Conventional Radiocarbon Age (BP)	Conventional Radiocarbon Age calibrated on calendar (% of probability)
Fa-2	Vallicella	organic sediment (bulk organic fraction)	AMS - Beta Analytic	14,040 +/− 40 BP	(95.4%) 15,368–15,030 cal BC (17317–16,979 cal BP)
Fa-3	Vallicella	organic sediment (bulk organic fraction)	AMS - Beta Analytic	7990 +/− 30 BP	(94.2%) 7049–6773 cal BC (8998–8722 cal BP)
					(1.2%) 6716–6706 cal BC (8665–8655 cal BP)
Fa-5	Vallicella	Charcoal (charred material)	AMS - Beta Analytic	4700 +/− 30 BP	(62.2%) 3474–3372 cal BC (5423–5321 cal BP)
					(24.8%) 3532–3486 cal BC (5481–5435 cal BP)
					(8.4%) 3623–3582 cal BC (5572–5531 cal BP)
Fa-6c	Vallicella	Charcoal (charred material)	AMS - Beta Analytic	4920 +/− 30 BP	(95.4%) 3769–3642 cal BC (5718–5591 cal BP)
Fa-8	Vallicella	organic sediment (bulk organic fraction)	AMS - Beta Analytic	7180 +/− 30 BP	(95.4%) 6076–5990 cal BC (8025–7939 cal BP)
Fa-10c	Vallicella	Charcoal (charred material)	AMS - Beta Analytic	3480 +/− 30 BP	(90.1%) 1888–1738 cal BC (3837–3687 cal BP)
					(5.3%) 1715–1696 cal BC (3664–3645 cal BP)
Fb-1c	Vallicella	Charcoal (charred material)	AMS - Beta Analytic	3520 +/− 30 BP	(95.4%) 1931–1749 cal BC (3880–3698 cal BP)
Fb-2c	Vallicella	Charcoal (charred material)	AMS - Beta Analytic	3200 +/− 30 BP	(95.4%) 1513–1416 cal BC (3462–3365 cal BP)
Fb-3c	Vallicella	Charcoal (charred material)	AMS - Beta Analytic	2240 +/− 30 BP	(69.1%) 321–202 cal BC (2270–2151 cal BP)
					(26.3%) 391–343 cal BC (2340–2292 cal BP)
Fb-4	Vallicella	organic sediment (bulk organic fraction)	AMS - Beta Analytic	6240 +/− 30 BP	(58.6%) 5306–5204 cal BC (7255–7153 cal BP)
					(36.8%) 5175–5067 cal BC (7124–7016 cal BP)
Fb-5	Vallicella	organic sediment (bulk organic fraction)	AMS - Beta Analytic	13,250 +/− 40 BP	(95.4%) 14,112–13,805 cal BC (16061–15,754 cal BP)
Fc-1	Vallicella	organic sediment (bulk organic fraction)	AMS - Beta Analytic	22,540 +/− 80 BP	(55.2%) 25,200–24,865 cal BC (27149–26,814 cal BP)
					(40.2%) 24,837–24,501 cal BC (26786–26,450 cal BP)
Fc-2c	Vallicella	Charcoal (charred material)	AMS - Beta Analytic	18,370 +/− 60 BP	(95.4%) 20,492–20,226 cal BC (22441–22,175 cal BP)
Fc-3	Vallicella	organic sediment (bulk organic fraction)	AMS - Beta Analytic	26,640 +/− 120 BP	(91.4%) 29,185–28,769 cal BC (31134–30,718 cal BP)
					(4.0%) 28,633–28,502 cal BC (30582–30,451 cal BP)
Fc-4	Vallicella	organic sediment (bulk organic fraction)	AMS - Beta Analytic	21,910 +/− 70 BP	(95.4%) 24,410–23,994 cal BC (26359–25,943 cal BP)
Fc-6c	Vallicella	Charcoal (charred material)	AMS - Beta Analytic	1870 +/− 30 BP	(92.8%) 116–239 cal AD (1834–1711 cal BP)
					(2.6%) 84–96 cal AD (1866–1854 cal BP)
Fd-1	Collemusino	organic sediment (bulk organic fraction)	AMS - Beta Analytic	5230 +/− 30 BP	(76.4%) 4065–3966 cal BC (6014–5915 cal BP)
					(13.3%) 4165–4129 cal BC (6114–6078 cal BP)
					(4.9%) 4223–4200 cal BC (6172–6149 cal BP)
					(0.8%) 4109–4102 cal BC (6058–6051 cal BP)
Fd-2	Collemusino	organic sediment (bulk organic fraction)	AMS - Beta Analytic	5060 +/− 30 BP	(95.4%) 3955–3783 cal BC (5904–5732 cal BP)
Fd-3	Collemusino	organic sediment (bulk organic fraction)	AMS - Beta Analytic	4440 +/− 30 BP	(47.9%) 3132–3007 cal BC (5081–4956 cal BP)
					(32.9%) 3331–3217 cal BC (5280–5166 cal BP)
					(7.6%) 2989–2930 cal BC (4938–4879 cal BP)
					(7.1%) 3188–3151 cal BC (5137–5100 cal BP)
Fd-4	Collemusino	organic sediment (bulk organic fraction)	AMS - Beta Analytic	7140 +/− 30 BP	(88.8%) 6067–5982 cal BC (8016–7931 cal BP)
					(6.6%) 5942–5926 cal BC (7891–7875 cal BP)
Fd-6	Collemusino	organic sediment (bulk organic fraction)	AMS - Beta Analytic	13,760 +/− 40 BP	(95.4%) 14,948–14,545 cal BC (16897–16,494 cal BP)
Fd-7	Collemusino	organic sediment (bulk organic fraction)	AMS - Beta Analytic	19,690 +/− 60 BP	(59.6%) 21,900–21,757 cal BC (23849–23,706 cal BP)
					(35.8%) 21,632–21,452 cal BC (23581–23,401 cal BP)
Fe-1	Collemusino	organic sediment (bulk organic fraction)	AMS - Beta Analytic	6610 +/− 30 BP	(66.2%) 5570–5481 cal BC (7519–7430 cal BP)
					(29.2%) 5620–5583 cal BC (7569–7532 cal BP)
Fe-3	Collemusino	organic sediment (bulk organic fraction)	AMS - Beta Analytic	7610 +/− 30 BP	(95.4%) 6502–6416 cal BC (8451–8365 cal BP)
Fe-4	Collemusino	organic sediment (bulk organic fraction)	AMS - Beta Analytic	14,500 +/− 40 BP	(95.4%) 15,937–15,500 cal BC (17886–17,449 cal BP)
Fe-6	Collemusino	organic sediment (bulk organic fraction)	AMS - Beta Analytic	14,040 +/− 40 BP	(95.4%) 15,368–15,030 cal BC (17317–16,979 cal BP)

acquisition rate varied from 50 to 60 scans/s depending on the terrain morphology. The horizontal resolutions achieved were 80 scans/m using the odometer and > 70 scan/m in time mode while the calculated vertical resolution was about 0.26 m. The GPR measures were georeferred by coupling with a geodetic Trimble R9s GPS receiver and integrated by using an odometric wheel. Post processing data analysis were performed by Radan (GSSI trademark) and ReflexW (Sandmeier Trademark) software and included horizontal and vertical filtering, deconvolution, migration and gain levelling. Reflection arrival times were converted in depth using averaged dielectric constant ranging from 9 to 17 and calculated from hyperbola diffractions occurring along the profiles. These values were used to perform time-to-depth conversions and migration along radargrams. The attenuation of electromagnetic waves amplitude due to the soil propagation limited the significance of signals to about 4 m (averaged) below the surface. Cross-examination between trench excavations and GPR layers depth showed good agreement with errors lower than 1–2%. The processed radargrams were topographically normalized to increase the effectiveness of the data overlay.

ERT and GPR surveys were purposely planned along overlapping profiles, so to better highlight subsurface discontinuities with different resolution (GPR ca. 4 m depth, ERT ca. 40 m depth) and from the analysis of different physical properties of the subsoil. Sub-vertical lateral variation in the stratigraphic record highlighted by both techniques have been commonly interpreted as faults juxtaposing different bodies (e.g., Roberts et al., 2010; Cinti et al., 2015), and have been further investigated through paleoseismological surveys.

The paleoseismological surveys were performed to constrain the nature of (i) potential fault scarps altered by anthropic activity, and (ii) discontinuities in the stratigraphic records shown by the geophysical surveys (Figs. 3a and 6a). The Vallicella site is characterized by a continuous trench about 156 m long and 2.5 m deep (Fig. 3a, c). The Collemusino site is characterized by two adjacent smaller trenches about 20 m (Trench 1) and 13 m (Trench 2) long and 2.5 m deep (Fig. 6a). In both sites, the trench depth was chosen to overcome the effect of the anthropic modification of the uppermost terrains. The trench depth limits the reconstruction of the seismic histories, as older and deeper evidence might be missed. The two different layouts were planned according to the different aims of the two investigation sites. In the Vallicella site, we performed a continuous trench to verify the nature of multiple potential fault scarps and geophysical discontinuities arranged across strike (Fig. 3a). In the Collemusino site, due to the preliminary available data and logistic reasons, we performed two small trenches directly on the surface projection of the discontinuities shown by the geophysical investigations (Fig. 6a). All the trenches have a benched layout, with one wall preserved vertically for interpretation. The trench walls have been surveyed to find evidence of surface-rupturing events, defined through the identification of colluvial wedges associated with fault scarps, upper terminations of fault splays and infilled coseismic fissures. The surveyed trench faces were framed with 1 m spaced grid on the fault zones, horizontal level lines connected by vertical lines every 2–5 m for the rest of the trenches, and several target points. Stratigraphic logs of the fault zones were carried both on tracing papers and photomosaics of the trench faces (e.g., McCalpin, 2009; Galli et al., 2011; McCalpin et al., 2023). Orthophotomosaics were generated from 24-megapixels photos captured by a Canon 850d camera and processed by structure-from-motion photogrammetry through Agisoft Metashape®. The reconstruction of the stratigraphic record was supported by radiocarbon dating of organic sediments and charcoal fragments, performed at the Beta Analytic Laboratory (Miami, FL, USA) (Table 1; see Supplementary Material S2 for details).

In addition to this, we constrained Late-Pleistocene throw-rates of fault splays by measuring the offset of dated paleosols found at multiple elevations along the fault escarpment and in a borehole (Fig. 2). The ages of these paleosols were obtained (i) during the surveys for the CARG geological sheet “348 Antrodoco” (Servizio Geologico d’Italia, 2022), which showed multiple paleosols both in outcrop and within the stratigraphy of a continuous-coring borehole dug in the hanging wall of the Mt. Marine fault, and (ii) from published paleoseismological studies on the Mt. Marine fault (Moro et al., 2002).

4. Results

Here we present the results obtained through our study, which allowed us to identify five main fault splays spread within an across-strike distance of about 500 m (Fig. 2). For each site, we present the results of the geophysical investigations and of the paleoseismological surveys.

4.1. Vallicella site

4.1.1. Geophysical survey

The ERT survey of the Vallicella site highlighted the presence of three lateral discontinuities in the 2-D subsurface electrical resistivity distribution down to a depth of about 20 m (A, B and C in Fig. 3a and b; see Supplementary Material S3 for the entire ERT cross-sections). The 2-D section shows a remarkable resistivity contrast characterized by a high-resistive layer (res > 600 Ωm) to the north-east laterally in contact with a layer with a significantly lower resistivity (res < 35 Ωm) to the south-west (discontinuity A in Figs. 3a, and b). About 30 m south of discontinuity A, the low resistivity body is abruptly interrupted against a high resistivity body (B in Fig. 3a and b). Southward of discontinuity B, we identified another lateral transition from a high resistivity body, located north-east of the discontinuity, and a low resistivity body located south-west of the discontinuity (C in Fig. 3a and b). These discontinuities match with the GPR radargram results in which we identify a low energy response (high attenuation of the EM signal) set amongst two well defined lateral dielectric contrast (Fig. 3b).

4.1.2. Paleoseismological survey

The Vallicella trench exposed three main normal faults, arranged both synthetic (Fault A and C, Fig. 3d) and antithetic (Fault B, Fig. 3d) to the principal Mt. Marine fault (Figs. 4 and 5; Fig. S4 in Supplementary Materials). The locations of the faults are consistent with the discontinuities shown by the geophysical surveys. Faults A and B form a graben structure in the uppermost sector of the trench about 44 m wide (Figs. 3d and 4a), meanwhile Fault C is in the lower sector of the trench, about 43 m south-west of Fault B (Fig. 3d). Several minor (throw <50 cm) synthetic and antithetic fault splays have been observed in the footwall of the three principal faults (see Fig. S4 in Supplementary Materials). In the next paragraphs we will firstly describe the stratigraphic setting of the trench, and secondly the paleoseismological analysis of the three main faults.

4.1.2.1. Stratigraphic setting. The Vallicella trench exhibited stratigraphy made of Upper Pleistocene alluvial fan deposits and Holocene colluvial deposits, as constrained by literature (Servizio Geologico d’Italia, 2022) and our own radiocarbon dating. We distinguished 12 stratigraphic units along the entire trench wall, whose order follows their stratigraphic position and radiocarbon ages. The most recent Unit 1 was found extensively along the entire trench wall (Figs. 4 and 5). It is a colluvial deposit made of brown gravelly silts highly altered by anthropic activity and enriched in charcoal and pottery shards. The colluvial nature of the unit implies that the age of Unit 1 may sensibly vary moving vertically within the unit. Due to the intense anthropic activity (ploughing and backfilling), the natural stratigraphic setting within the unit is compromised, and therefore sample dating may provide ages that will not reflect their original stratigraphic position. Only in proximity of Fault C we identified a portion of Unit 1 that most likely is preserved by ploughing and backfilling (Sub-Unit 1a; Fig. 5c). Radiocarbon dating of a charcoal fragment collected in Sub-Unit 1a

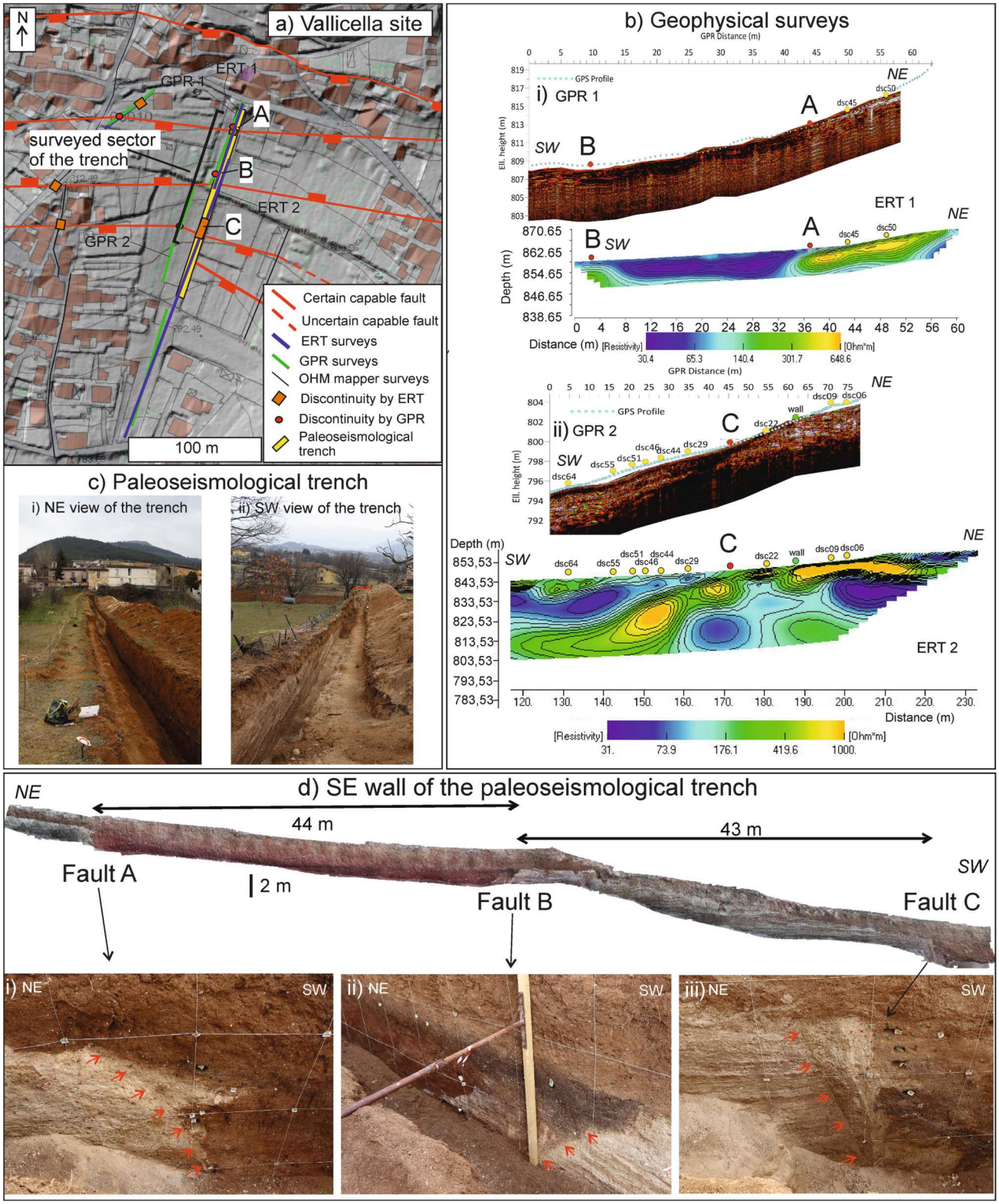

Fig. 3. The Vallicella site. A) Location map of the site: in yellow is the paleoseismological trench, in blue are the ERT surveys, in green are the GPR surveys, in black the Ohm mapper surveys. The black bar highlights the sector of the trench that we were able to survey. B) Geophysical surveys. Yellow and red circles are minor and major discontinuities shown by the GPR surveys, respectively. It is shown how both the GPR and ERT have provided consistent locations of major discontinuities in the geophysical record (marked with A, B and C and reported also in map view in Fig. 3a). C) Panoramic photos of the trench. D) Photomosaic of the south-eastern wall of the trench; with A, B and C are reported the locations of the discontinuities shown by the geophysical surveys, which correspond to three faults: Fault A (Fig. 3d.i); Fault B (Fig. 3d.ii); Fault C (Fig. 3d.iii). The red arrows mark the principal fault planes. See Fig. S1 for the entire ERT sections and Fig. S4 for the photomosaic of the entire trench wall (Supplementary Materials). (For interpretation of the references to colour in this figure legend, the reader is referred to the web version of this article.)

provides an age of 116–239 CE (Sample Fc6c, Fig. 5c).

Below Unit 1, we have identified a set of stratigraphic units infilling the graben between Fault A and Fault B, Holocene (Units 2–5) and Late Pleistocene (Units 6–7) in age, and a set of Late Pleistocene units located in the hanging wall of Fault C (Units 8–11), where it is present also the younger Unit 3/5a. We will now describe firstly the younger set of stratigraphic units, belonging to the infilling of the graben between Fault A and B, and secondly the older units, located in proximity of Fault C.

Unit 2 is a colluvial deposit made of blackish-brown silts enriched in organic material, charcoal, and pottery shards (Figs. 4a, b and 5b). This unit seals the entire graben between Fault A and B, with its thickness increasing moving downhill towards Fault B (Figs. 4a and 5b). Radiocarbon dating of a charcoal fragment provided an age of 1513–1416 BCE for Unit 2 (sample Fb2c, Fig. 5b). Radiocarbon bulk dating of organic sediments obtained in the thickened sector of the unit provided sensibly older ages (5306–5204 BCE, Sample Fb4, Fig. 5b). Given the potential contamination of the latter with older material coming from the dismantled scarp associated with Fault B, we tend to discard the sample Fb4.

Unit 3 is a colluvial deposit made of dark reddish-brown silts with scarce-to-frequent centimetric clasts, both of carbonate and cherty nature. Radiocarbon dating of a charcoal fragment provided an age of 1888–1738 BCE (sample Fa10c, Fig. 4b), and the bulk organic fraction of a second sample provided a radiocarbon age of 3474–3372 BCE (sample Fa5, Fig. 4c). We consider 1888–1738 BCE as the age of Unit 3, as older ages of sample Fa5 most likely result from contamination of the sample with older material located within the colluvial unit.

Unit 4 is a buried paleosol formed by blackish silt with scarce-to-frequent centimetric clasts, enriched in organic material and charcoal and pottery shards. Charcoal dating provided an age of 3769–3642 BCE (sample Fa6c, Fig. 4c).

Unit 5 represents most of the infilling of the graben between Fault A and Fault B. Overall, it is characterized by dark reddish-brown silts and silty clays, with strongly weathered sub-centimetric carbonate clasts. The high decarbonation of the clasts and the presence of polyhedral structures suggest that this unit has been affected by intense pedogenesis. Bulk dating of organic sediment in proximity of Fault A provided ages of 7049–6773 BCE (Sample Fa3, Fig. 4b) and 6076–5990 BCE (sample Fa8, Fig. 4c). In proximity of Fault B, the transition from Unit 5 to Unit 2 is gradual. In this sector, we dated a charcoal fragment collected in the uppermost section of unit 5, which provided an age of 1931–1749 BCE (Sample Fb1c, Fig. 5b), suggesting that the unit spans across a large age range.

Unit 6 is in the hanging wall of Fault B. It is characterized by highly weathered sands and gravels interbedded with paleosol horizons (Fig. 4a and 5b). We also discretized Unit 6a in the lowermost part of Unit 6 as a layer of brown reddish silts without clasts (Fig. 4a and 5b). Bulk dating of Unit 6a provided an age of 14,112–13,805 BCE (Sample Fb5, Fig. 5b).

Unit 7 is located at the bottom of the trench wall (Fig. 4a). It is composed of highly weathered gravels and sands with centimetric clasts, arranged in thin layers alternated with paleosol horizons. Although the similarity between Units 6 and 7, the poor exposure of Unit 7 did not allow us to accurately define the relationships between these two sedimentary bodies, and therefore we decided to keep them as two separate units.

The older stratigraphic units (8–11) are in the hanging wall of fault C. These are mostly characterized by colluvial deposits draping the hanging wall of the fault scarp above Unit 12, the older unit found in the trench.

Unit 8 is a brown-orange silty-sandy colluvial deposit, with rare white millimetric clasts.

Unit 9 is a massive brownish-greyish sandy gravel, with subangular clasts sized up to 5 cm. Bulk dating of organic material dispersed in the unit provided an age of 24,410–23,994 BCE (Sample Fc4, Fig. 5c). Considering the age of the older unit below (see next) and the colluvial nature of the deposit, we believe this age may be biased by contamination with older colluviated sediments.

Unit 10 is a sandy-silty clay colluvium, with centimetric angular-subangular clasts. Bulk dating of sediment yielded an age of 29,185–28,769 BCE (sample Fc3, Fig. 5c), meanwhile charcoal dating provided an age of 20,492–20,226 BCE (sample Fc2c, Fig. 5c). Given the colluvial nature of the unit, we consider more reliable the younger age, with the older age most likely derived from older material deposited into the colluvial deposit.

Unit 11 is a brownish-blackish silty gravel colluvium, with centimetric clasts, rich in organic material. Bulk dating of the organic matrix provided an age of 25,200–24,865 BCE (Fc1, Fig. 5c).

This set of colluvial units is sealed by Unit 3/5a, which lies in onlap above Unit 8. This unit is made by decimetric sub-horizontal layers and lenses of gravels and silty sands, and it could be interpreted as an alluvial fan deposit. Although we could not perform dating of this unit, we hypothesize that it could be coeval to Units 3 to 5, given its stratigraphic position and facies. In this scenario, Unit 3/5a will therefore represent the distal part of a Holocene alluvial fan, meanwhile Units 3 to 5 represent colluvial deposits heteropic to the Holocene alluvial fans.

Unit 12 is the stratigraphically oldest unit in the trench. This is generally formed by gravel deposits having similar lithology, texture and structure recognized in nearby alluvial fans dated Late Pleistocene (Servizio Geologico d'Italia, 2022). We identified this unit in the footwall of the three faults. Specifically, in the footwall of Fault A, Unit 12 is characterized by beige sandy gravels of carbonate angular-subangular centimetric clasts, poorly layered. Between Fault B and C, Unit 12 is made mainly by whitish sandy gravels, with centimetric subangular-subrounded clasts arranged mostly in horizontal layers interbedded with sandy layers. We have also identified Unit 12a in the hanging wall of Fault C. This sub-unit has similar lithology and texture of Unit 12, but we do not have elements to directly correlate it with the layers of Unit 12 present in the footwall of Fault C. We guess that Unit 12a could represent the uppermost part of the original Unit 12.

4.1.2.2. Fault A. Fault A is characterized by a principal SW-dipping normal fault (F1; attitude 223/63 in dip direction/dip), associated with minor splays located both in the hanging wall and the footwall of F1 (Figs. 3d and 4). As in this sector both the trench walls were well preserved, we have logged them both (Fig. 4). Overall, we have identified four surface-rupturing paleoevents.

The most-recent event (ev1A-MRE) is suggested by the offset of the base of Unit 1 along minor fault splays in the footwall of F1 (F2f and F3f in Fig. 4b and c). The measured offset is 12 cm, and this represents a minimum value, due to the large anthropic rework that characterized the entire Unit 1 and probably erased the original topographic surface at the time of the surface faulting. In fact, we suggest that ploughing and backfilling have erased evidence of coseismic ruptures along F1, which instead survived on the minor footwall splays likely because carved in gravels, more resistant to erosion than colluvial deposits of F1. This event occurred after the age of Unit 3 (1888–1738 BCE, Sample Fa10c; Fig. 4c).

An older surface-rupturing event (ev2A) caused the formation of the colluvial wedge CW1 (Figs. 4b, c). The coseismic throw of ev2A could vary from a minimum of 60 cm, provided by the thickness of CW1, up to a maximum of 120 cm, assuming that the coseismic throw is double the thickness of CW1 (e.g., McCalpin, 2009). The western wall shows that CW1 lies within Units 3 and 4. Hence, ev2A occurred between 3769 and 3642 BCE (Sample Fa6c, Unit 4) and 1888–1738 BCE (Sample Fa10c, Unit 3; Fig. 4c).

In the lowermost part of the trench wall, we identified an older colluvial wedge (CW2; Fig. 4b, c). The latter is clearly faulted on the eastern wall, suggesting therefore the occurrence of two older surface-rupturing events, one that faulted CW2 (ev3A) and a previous one that formed CW2 (ev4A). Ev3A produced 70 cm of throw of CW2 along a synthetic hanging wall splay of F1 (Fig. 4b). The thickness of CW2

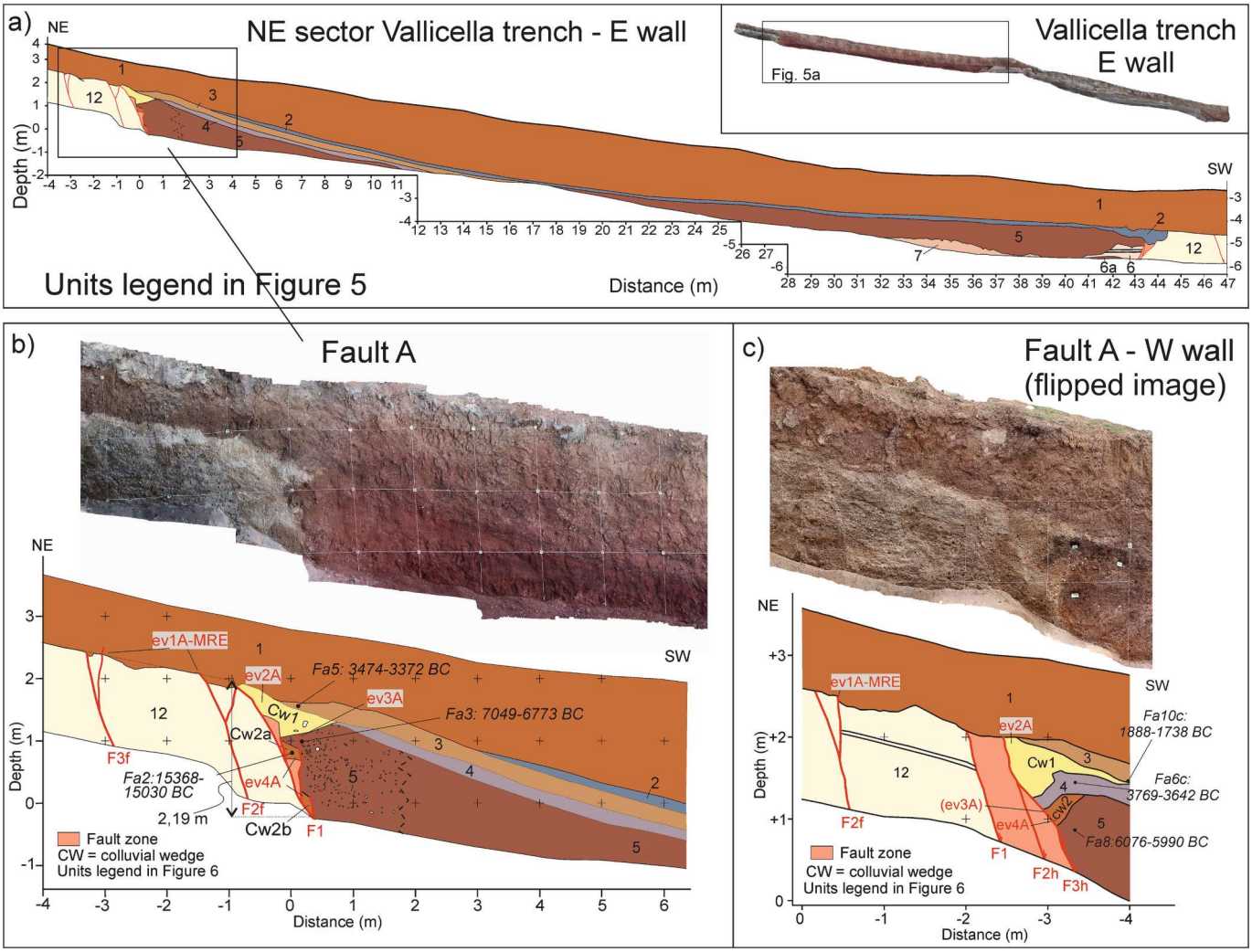

Fig. 4. Paleoseismological record of the NE sector of the Vallicella trench and Fault A. A) Stratigraphic log of the graben structure present in the NE sector of the trench. The insight map shows its location in respect of the entire surveyed trench. B) Stratigraphic log of Fault A, SE wall. C) Stratigraphic log of Fault A, NW wall (image flipped for comparison). The legend of the stratigraphic units is shown in Fig. 5.

suggests instead a minimum throw for ev4A of about 30 cm, up to a maximum of 60 cm (Figs. 4b, c). The western wall shows that CW2, i.e., ev4A, occurred after the sample Fa8 (6076–5990 BCE; Unit 5) and before the deposition of Unit 4, dated 3769–3642 BCE (sample Fa6c). We have no direct evidence of the relationships between ev3A and Unit 4. However, ev3 is clearly sealed by CW1, suggesting therefore that ev3A occurred prior to its deposition. Hence, both ev3A and ev4A occurred between 6076 and 5990 BCE (Unit 5) and 3769–3642 BCE (Unit 4).

4.1.2.3. Fault B. Fault B is characterized by two main NE-dipping fault splays with attitude 057/55, displacing the hanging wall Holocene colluvial sequence onto the footwall Late Pleistocene alluvial fan gravels (Fig. 5b). We have identified the occurrence of one surface-rupturing event (ev1B-MRE). This event faulted the organic-rich Unit 2, that is the earthquake horizon of ev1B-MRE. Above the upper termination of F1, we identified a sub-vertical slope which puts in contact Unit 2 with Unit 12, which represents a retreated free-face generated by the surface-rupturing event. Unit 2 is partially resedimented in the hanging wall of F1, due to the dam-like effect caused by this counterslope scarp. Due to this and to the alteration of the top of Unit 2 following the deposition of Unit 1 and its anthropic modification, we felt more confident to measure the offset of ev1B-MRE by projecting the undisturbed base of Unit 2, taken away from the fault, against the vertical scarp. This allows us to measure 22 cm as the minimum throw associated with the surface-rupturing event (see dashed line in Fig. 5b). The event occurred after 1931–1749 BCE (Sample Fb1c, top of Unit 5) and before 321–202 BCE (Sample Fb3c; Fig. 5b). That is because, although the anthropic activity that sensibly altered Unit 1 may have modified the original stratigraphic position of sample Fb3c, ev1B-MRE does not appear to have ruptured the base of Unit 1, as it instead occurred along Fault A. Hence, we can assume that the surface-rupturing event occurred before the deposition of sample Fb3c.

4.1.2.4. Fault C. Fault C is characterized by a main SW-dipping fault zone (F1-F2) with attitude 224/75 and a set of nearly vertical, slightly NE-dipping pseudo-reverse fault strands cutting across the colluvial deposits in the hanging wall of F2 (F3, F4, F5; Fig. 5c). We have identified evidence of at least three surface-rupturing paleoevents. The most recent one (ev1C-MRE) has faulted the entire stratigraphic succession along F2 and F3. The cumulative minimum offset associated with ev1C-MRE is about 29 cm. The anthropogenic nature of Unit 1 and of its base prevents any reconstruction of the original free face height. The faulting of Unit 1a testifies that the event occurred after 116–239 CE (Sample Fc6c, Fig. 5c).

The penultimate event, ev2C, caused the formation of an open fissure and a colluvial wedge (CW) in the hanging wall of F2, and the offset of

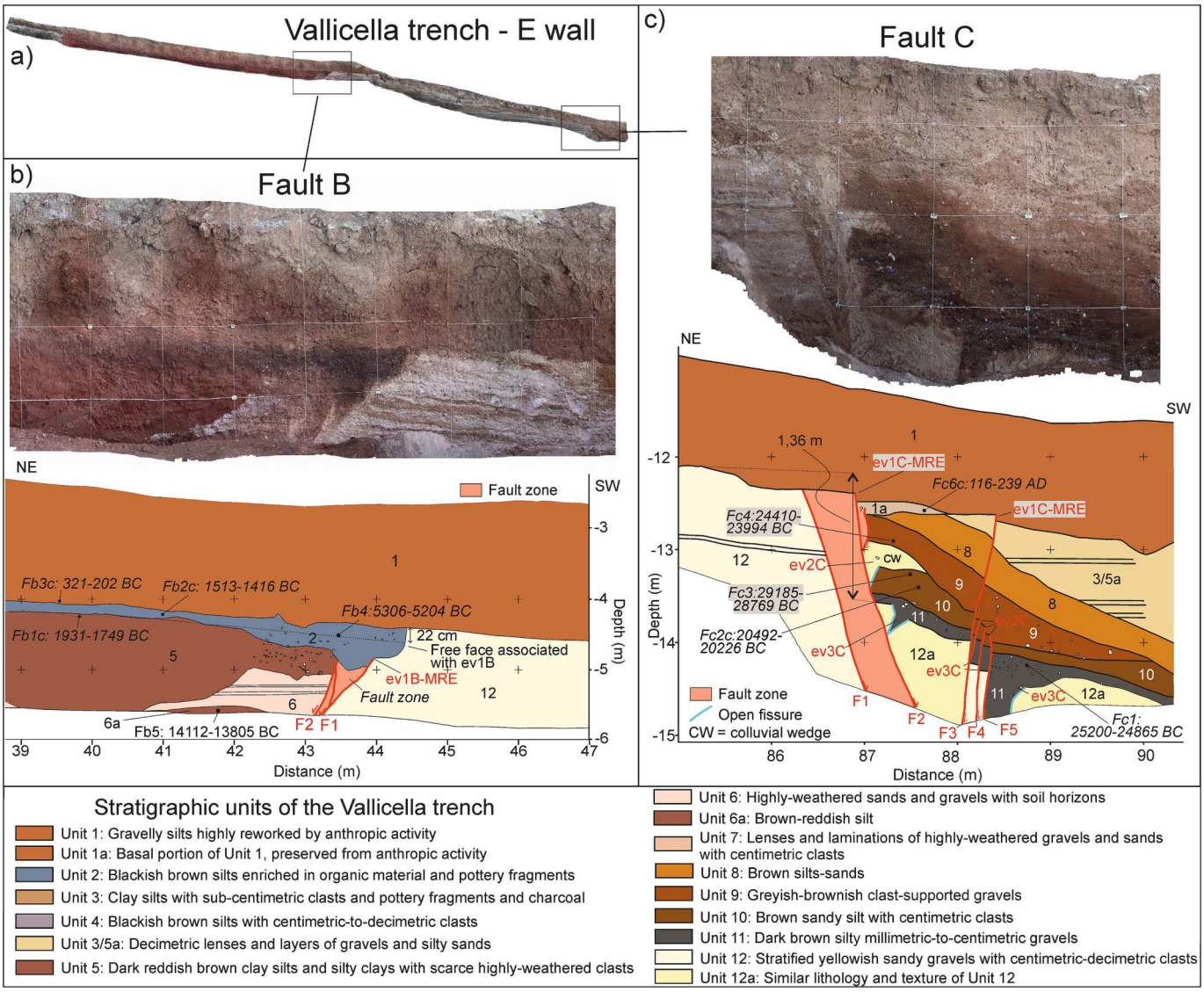

Fig. 5. Stratigraphic logs of Faults B and C. A) Insight map showing the location of the faults in respect of the entire trench. B) Stratigraphic log of Fault B. C) Stratigraphic log of Fault C.

the top of Unit 10 along all the hanging wall splays F3–5. We therefore interpret the top of Unit 10 as the earthquake horizon of ev2C. The coseismic throw associated with F2 varies from a minimum of 30 cm up to a maximum of 60 cm, provided by the thickness of CW; the cumulative throw measured on the hanging wall fault splays is also about 30 cm. Therefore, the minimum coseismic throw for ev2C is about 60 cm. Considering the stratigraphic consistency of the obtained ages, we can constrain this event to have occurred after 20,492–20,226 BCE (Sample Fc2c, Unit 10; Fig. 5c). Given its position at depth combined with the upper termination of a small fault splay in the hanging wall of F2, it is possible that CW has been downthrown by at least one more surface-rupturing event. However, we do not have stratigraphic constraints to infer the age and offset associated with this event.

The older earthquake found on Fault C (ev3C) caused the opening of hybrid fissures in the hanging wall of both F2 and F5, showing components of both horizontal opening and vertical movement, filled with Unit 11 (Fig. 5c). We have no elements to quantify the offset on F2, therefore we can establish a minimum coseismic throw associated with ev3C of 40 cm based solely on the offset measured along the hanging wall splays and the hybrid fissures. As Unit 11 represents the infilling of the fissures, we hypothesize that the ev3C could be coeval or younger than the age of Unit 11 (25200–24,865 BCE, Sample Fc1).

4.2. *Collemusino site*

4.2.1. *Geophysical survey*

The ERT survey performed in the Collemusino site have highlighted the presence of two lateral passages between high resistivity and low resistivity bodies (Fig. 6). Specifically, in correspondence of D a high resistivity body is abruptly interrupted towards south against a low resistivity body (Fig. 6a and b). About 50 m south of D, the low resistivity body again passes laterally to a higher resistivity body (E in Fig. 6a and b). The GPR surveys have identified two lateral passages of radar facies as well, and their locations are consistent with those obtained through the ERT surveys.

4.2.2. *Paleoseismological survey*

The two paleoseismological trenches performed in the Collemusino site have confirmed the presence of surface-rupturing faults in correspondence with the discontinuities identified by the geophysical surveys

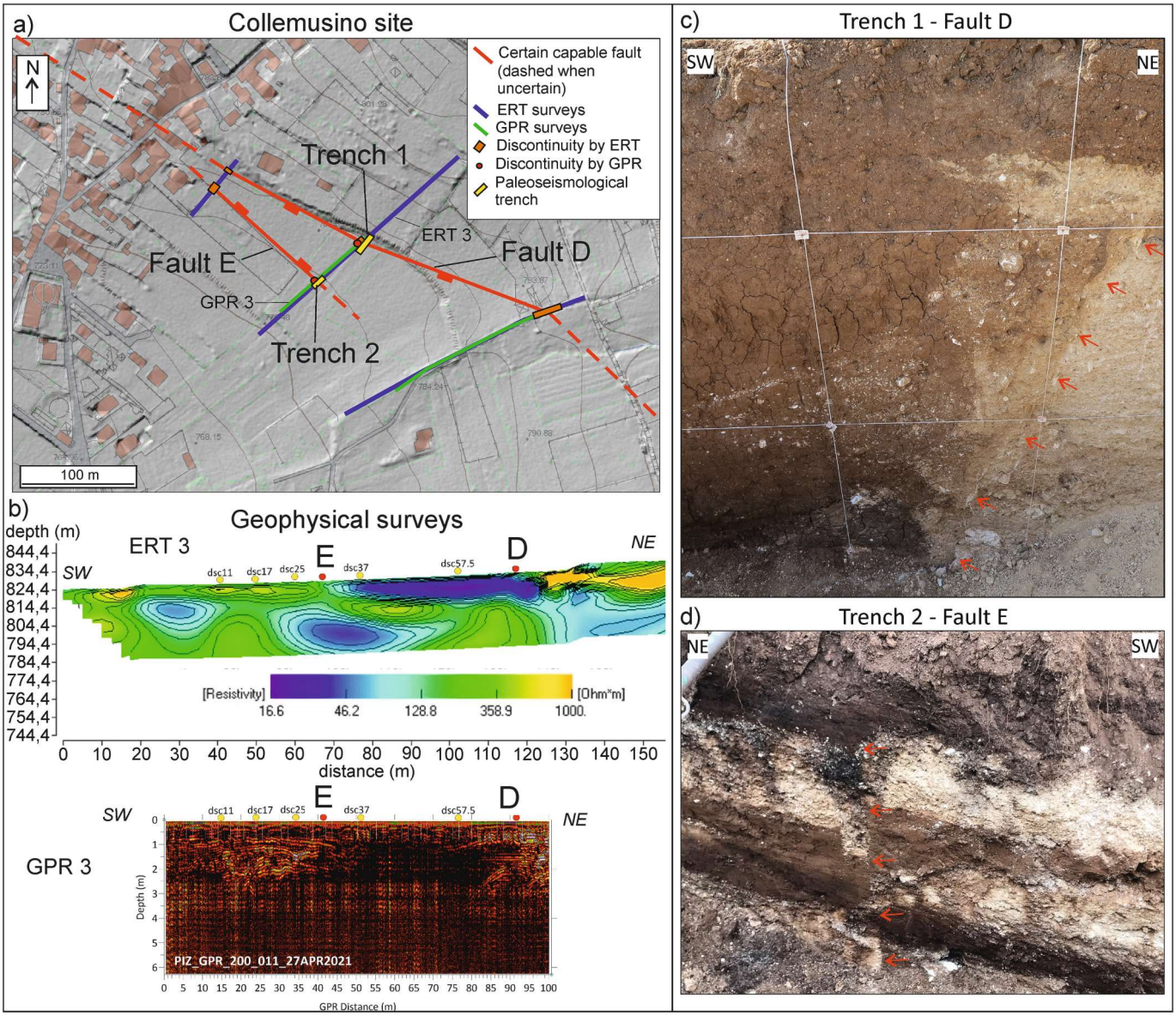

Fig. 6. The Collemusino site. A) Location map of the site: in yellow are the paleoseismological trenches, in blue are the ERT surveys, in green are the GPR surveys. B) Geophysical surveys. Yellow and red circles are minor and major discontinuities shown by the GPR surveys, respectively. It is shown how both the GPR and ERT have provided consistent locations of discontinuities in the geophysical record (marked with D and E and reported also in map view in Fig. 6a). C) Photos of the two faults found within the trenches; the red arrows mark the principal faults. See Fig. S3 in Supplementary Materials for the entire ERT section. (For interpretation of the references to colour in this figure legend, the reader is referred to the web version of this article.)

(Fig. 6c and d). Trench 1 exhibited a SW-dipping fault (Fault D; Fig. 7a), synthetic to the main Mt. Marine fault, meanwhile Trench 2 exhibited an antithetic NE-dipping fault (Fault E; Fig. 7b) located about 53 m SW of Fault D. In the next paragraphs the analysis of both trenches is described.

4.2.2.1. Trench 1

4.2.2.1.1. Stratigraphic setting. We have identified five different Late Pleistocene-Holocene stratigraphic units (Fig. 7a). The most recent is Unit 1, a chaotic colluvial deposit highly reworked by anthropic activity and enriched in pottery shards and charcoal fragments. Below Unit 1, we have distinguished a set of colluvial units (Units 2–4) located in the hanging wall of Fault D, and an older stratigraphic unit located in the footwall of the fault (Unit 5).

Unit 2 is a very dark grey silty sands with dark clasts, pottery shards and charcoal fragments located in the fault hanging wall. Dating of the bulk organic fraction within the sediments provides an age of 3955–3783 BCE (Sample Fd2, Fig. 7a). This unit gradually passes below to Unit 3.

Unit 3 was subdivided into three sub-units according to their texture and ages. Sub-Unit 3a is a sandy silty reddish-brown colluvial deposit with sub-centimetric clasts and frequent volcanic minerals. Bulk dating of organic sediment in Sub-Unit 3a provided an age for the upper part of the unit of 4065–3966 BCE (Sample Fd1, Fig. 7a). Sub-Unit 3b is a brown sandy-silty colluvial deposit with centimetric carbonatic clasts, locally weathered by pedogenic processes, and volcanic minerals. This sub-unit has a wedged-shaped geometry, thicker towards the fault and thinning towards the hanging wall, and it is in heteropic contact with Sub-Unit 3c (Fig. 7a). We have no radiocarbon ages for Sub-Unit 3b. Sub-Unit 3c is a sandy-silty brown colluvium, for which bulk radiocarbon dating of organic sediment located in the lower part of the wall provided an age of 21,900–21,757 BCE (Sample Fd7; Fig. 7a). Given the stratigraphic relationships between 3b and 3c, we infer that Sub-Unit 3b belongs to the Late Pleistocene, most likely towards the passage to the Holocene.

Unit 4 is a dark reddish-brown clay-silty paleosol, with

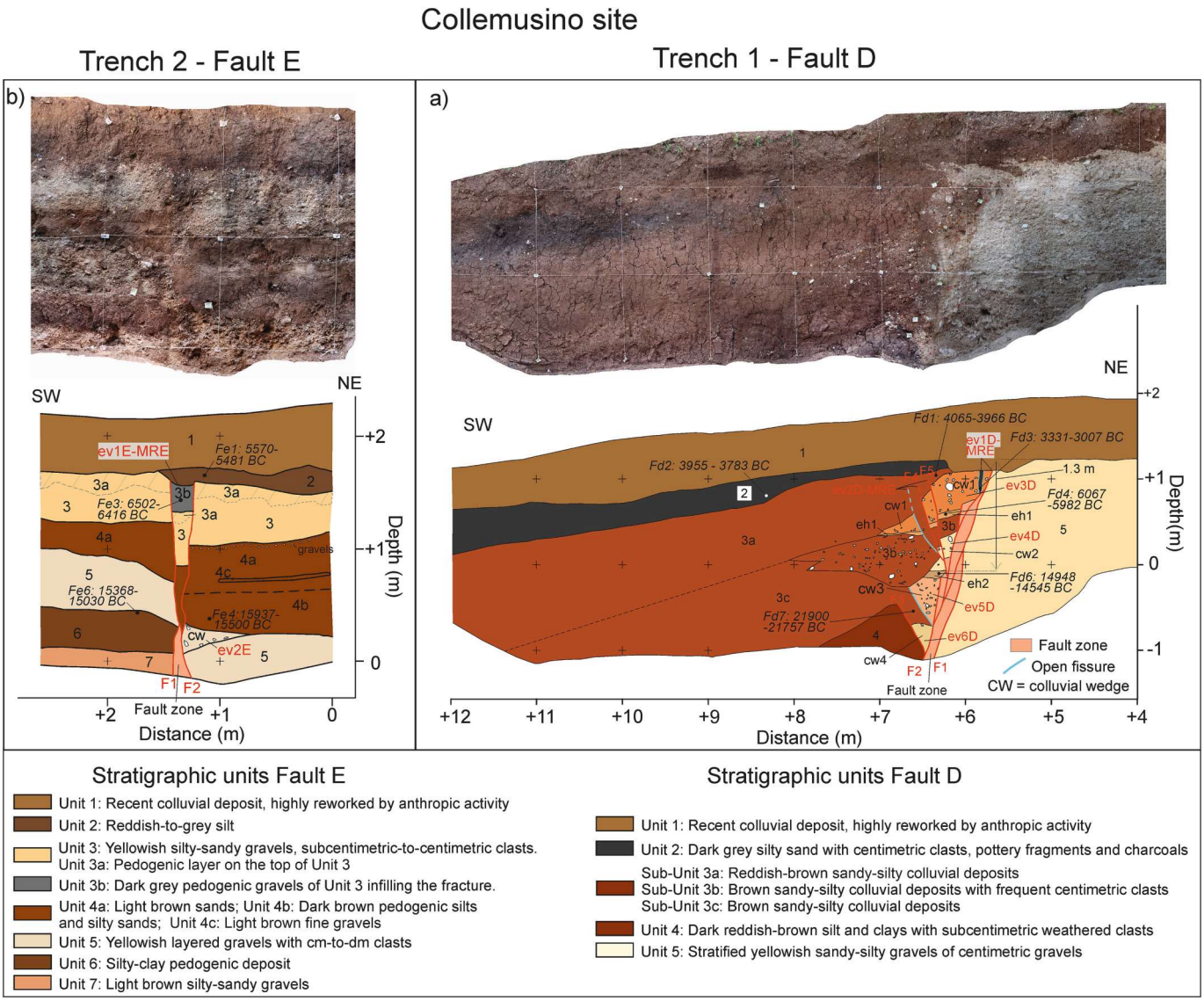

Fig. 7. Paleoseismological record of the Collemusino site. A) Stratigraphic log of Fault D. B) Stratigraphic log of Fault E.

subcentimetric clasts altered by pedogenic processes (Fig. 7a). We have no radiocarbon ages for this unit. Provided its position in the stratigraphic record, we can infer that this unit belongs to the Late Pleistocene.

Unit 5 is the oldest unit found in Trench 1, in the footwall of fault D (Fig. 7a). It is characterized by alluvial fan deposits made of sandy-silty gravels with angular-subangular centimetric clasts, poorly stratified and an overall SW-dipping attitude. This unit can be referred to the Late Pleistocene, by comparison with ages of similar alluvial fan deposits observed in the Vallicella trench.

4.2.2.1.2. Fault D. Fault D is characterized by a main SW-dipping fault with attitude 216/66 and a set of minor splays and open fissures in its hanging wall (Fig. 7a). Within this fault zone, we identified evidence of six surface-rupturing paleoevents. The most recent event (ev1D-MRE) faulted the entire stratigraphic record along the main fault (F1-F2) and caused the opening of a fissure within CW1 which was filled by Unit 2. It was not possible to determine the offset along the main fault. The high organic content of the infilling of the fissure within CW1 might suggest that it was the soil at the time of the surface-rupturing event, later colluviated within the open fissure. Therefore ev1D-MRE could have occurred close or after the age of the dated sample (3331–3007 BCE, Sample Fd3).

The penultimate event ev2D is determined by faulting of CW1 along hanging wall splays F4 and F5, and by the opening of a hybrid fissure within CW1 and Unit 3b. The minimum coseismic throw of ev2D provided by the hanging wall splays is 10 cm. Most likely the earthquake ruptured also along the main fault, but we have no evidence to constrain this. The fissure is filled by Unit 3a, indicating that the event must at least be synchronous to Unit 3a. However, the upper terminations of F4 and F5 were not clearly definable in the field, most likely being altered by pedogenic processes in Units 2 and 3a. Hence, it is difficult to establish whether ev2D occurred before or after sample Fd1. As the base of Unit 2 is not faulted, we feel more confident to constrain ev2D to be older than Unit 2.

The colluvial wedge CW1 testifies the occurrence of an older event, ev3D. The thickness of CW1 is 45 cm, which suggests that the coseismic throw varies between 45 cm and 90 cm. The wedge lies above a paleosol level which we interpret as the earthquake horizon for ev3D (eh1). The age of eh1 provides therefore the *post quem* term for ev3D, which is 6067–5982 BCE (Sample Fd4). The *ante quem* term of the event is provided instead by the sample Fd1, aged 4065–3966 BCE (top of Unit 3a), collected in the sediment deposited just above CW1.

An older colluvial wedge (CW2) testifies the occurrence of an older surface-rupturing event, ev4D. The thickness of CW2 is about 27 cm,

which suggests the coseismic throw to vary between a minimum of 27 cm and a maximum of 54 cm. Dating of pedogenic deposits collected underneath CW2, which we interpreted as the earthquake horizon for ev4D (eh2), provided a *post quem* term of the earthquake of 14,948–14,545 BCE (Sample Fd6). The *ante quem* term of the event is provided by sample Fd4, dated 6067–5982 BCE.

An older event (ev5D) is testified by an open fissure in the hanging wall of the main fault, infilled with material whose lithology and texture resemble the one of a colluvial wedge sourced by the footwall gravels. We therefore interpret the infilling material as part of a colluvial wedge that filled the fissure opened by ev5D and then was subsequently eroded, hence only its portion within the fissure remain preserved (CW3). We have no data for defining the coseismic throw associated with this earthquake. The fissure is clearly sealed by eh2, so the event must have occurred before 14,948–14,545 BCE (Sample Fd6). The fissure opened within Unit 3c, hence ev5D must have occurred after Sample Fd7 (21900–21,757 BCE, bottom of Unit 3c).

The oldest event we identified on Fault D is ev6D, which caused the onset of a colluvial wedge (CW4) faulted along the main fault and an antithetic hanging wall fault splay (F3). We have no elements for constraining the coseismic throw, due to the intense faulting of CW4 along both splays. This wedge is sealed by Sub-Unit 3c, and therefore the event occurred before 21,900–21,757 BCE (Sample Fd7).

4.2.2.2. Trench 2

4.2.2.2.1. Stratigraphic setting. We have identified seven stratigraphic units in Trench 2, belonging to Late Pleistocene alluvial fans and Late Pleistocene-Holocene eluvial-colluvial deposits (Fig. 7b). Moving from the most recent unit, we identified Unit 1 as historical colluvium made by clayey silts with carbonate clasts, highly reworked by anthropic activity.

Unit 2 is located above the fault zone, and it increases its thickness moving NE (Fig. 7b). It is a colluvial deposit composed of dark reddish brown and very dark grey silts with scarce clasts, most likely originated by reworking of the older Unit 3a. Dating of the bulk organic fraction within the sediment provided an age for this unit of 5570–5481 BCE (Sample Fe1; Fig. 7b).

Unit 3 is characterized by silty-sandy gravels, with subcentimetric-to-centimetric clasts, locally weathered by pedogenic processes. In the upper portion of this unit, the pedogenesis is more intense, and so we have defined the Sub-Unit 3a as a paleosol developed on top of Unit 3. The latter filled up a fissure along Fault E, and we identified the infilling material as a different Sub-Unit 3b, made of dark grey gravels from Unit 3 with abundant organic-rich matrix (Fig. 7b). The bulk organic fraction within the sediment was dated 6502–6416 BCE (Sample Fe3).

Unit 4 has been subdivided into three different sub-units, according to their lithology and texture. Sub-Unit 4a is made of dark brown silts and silty sands of colluvial origin, altered by pedogenic processes. On top of Sub-Unit 4a there is a horizon of gravels made of centimetric carbonate subrounded clasts. Sub-Unit 4b is characterized by light brown massive sands and silty sands with scarce subcentimetric clasts. Sub-Unit 4c is a lens of fine gravels with clasts up to 1–2 cm. Sub-Units 4b and 4c are found only in the fault hanging wall, where Unit 4 reaches a maximum thickness of about 85 cm, meanwhile Sub-Unit 4a is found in both hanging wall and footwall, where it reaches a maximum thickness of 55 cm. Bulk dating of organic material in Sub-Unit 4b provided an age of 15,937–15,500 BCE (Sample Fe4). As this age is older than the age of the units underneath (see next), we consider this age contaminated by old deposits colluviated within the unit.

Unit 5 is made of gravels with centimetric, subangular-subrounded clasts arranged in sub-horizontal layers.

Unit 6 is a dark reddish-brown clay-silty paleosol found only in the footwall of the fault. In the upper portion, the silty fraction becomes predominant, and the unit embeds subcentimetric clasts. Bulk dating of organic sediment provided an age for the unit of 15,368–15,030 BCE (Sample Fe6).

The oldest unit we identified is Unit 7, made of silty-sandy gravels with subangular centimetric clasts.

4.2.2.2.2. Fault E. Fault E is characterized by two sub-vertical NE-dipping fault splays (134/89). We identified evidence of two surface-rupturing paleoevents (Fig. 7b). The most recent one (ev1E-MRE) faulted the entire stratigraphy before being sealed by Unit 2. The earthquake caused the collapse of the stratigraphy within F1 and F2, which has then been infilled by Unit 3b. Assuming that the latter represents the soil at the moment of the earthquake, the age of Unit 3b shortly predates ev1E-MRE. Hence, the event occurred after 6502–6416 BCE (Sample Fe3, Unit 3b) and prior to 5570–5481 BCE (Sample Fe1, Unit 2). The coseismic throw associated with ev1E-MRE is about 20 cm, measured as the vertical offset of the interface between Units 3 and 4a. A colluvial wedge (CW) found at the base of the trench wall highlights the occurrence of another event (ev2E) along Fault E. The CW lies on top of Unit 5, and it is made of the same rock material of Unit 5 itself. Moreover, the top of Unit 5 in the footwall seems to have been eroded in proximity of the fault (Fig. 7b). Therefore, we suggest that CW is formed by the dismantling of the fault scarp created by ev2E in Unit 5. The measured coseismic throw of ev2E is 55 cm, resulting from the throw of the top of Unit 5 minus the throw due to ev1E-MRE. This throw value corresponds also to the double of the thickness of CW (about 26 cm). Sample Fe6 (Unit 6) constrains the earthquake to have occurred after 15,368–15,030 BCE.

5. Throw-rates of the Mt. Marine fault

The estimated multi-temporal throw-rates of the Mt. Marine fault were derived from our paleoseismological surveys (Figs. 4b, 5c, 7a) and from the offsets of multiple paleosols along the overall fault escarpment (Fig. 8; Table 2).

In terms of the paleoseismological throw-rates, we estimated values associated with the main synthetic fault splays by restoring dated stratigraphic horizons found in the hanging wall of the fault to the top of the footwall, underneath Unit 1 of both Vallicella and Collemusino sites (see Figs. 4b, 5c, 7a). These throw-rates represent a minimum value, as the footwall of the faults has been intensively eroded over time and the same dated layers were not preserved in the footwall. We obtained a minimum throw-rate of 0.3 mm/yr for the last 8 kyrs on Fault A, 0.05 mm/yr for the last 25 kyrs on Fault C and 0.08 mm/yr for the last 15 kyrs on Fault D. Bearing in mind that these values may be intensively influenced by erosional processes, they suggest that Fault A hosts the largest throw-rate at least over the last 8 kyrs.

As mentioned above, paleoseismological throw-rates may be hindered by erosional processes, and therefore they may not be fully representative of the cumulative throw and throw-rates of the faults. This is due to the limited depth of the paleoseismological trenches, which did not allow to identify the same lithostratigraphic reference level both in the hanging wall and footwall of the faults. In order to obtain values that better approximate the fault behaviour, we estimated throw-rates by correlating dated paleosols embedded in alluvial fan deposits outcropping along the prominent fault escarpment in the Vallicella area (Fig. 8). Specifically, in the immediate footwall of Fault A a set of paleosols dated about 40 ka (Sample FP250) and 29 ka (Sample FP137) crops out. A paleosol found within the paleoseismological trench performed by Moro et al. (2002), located between Fault B and Fault C, is dated about 35 ka (Sample PIZ4). In addition to this, the stratigraphy of a 28 m-deep borehole highlights the presence of a buried paleosol dated about 35 ka at 15 m depth, located in the immediate hanging wall of Fault C (Sample VAL-15/1; see S5 in Supplementary Materials for details on the stratigraphy of the borehole).

Paleosols FP250 and FP137 embed layers deposited by alluvial fans. Given the episodic sedimentation of these layers, we have no elements to ascertain the exact depth of a layer dated 35 ka in between the two paleosols. Therefore, we assume that an intermediate layer dated 35 ka is located half-way FP250 and FP137. The throw between this layer and

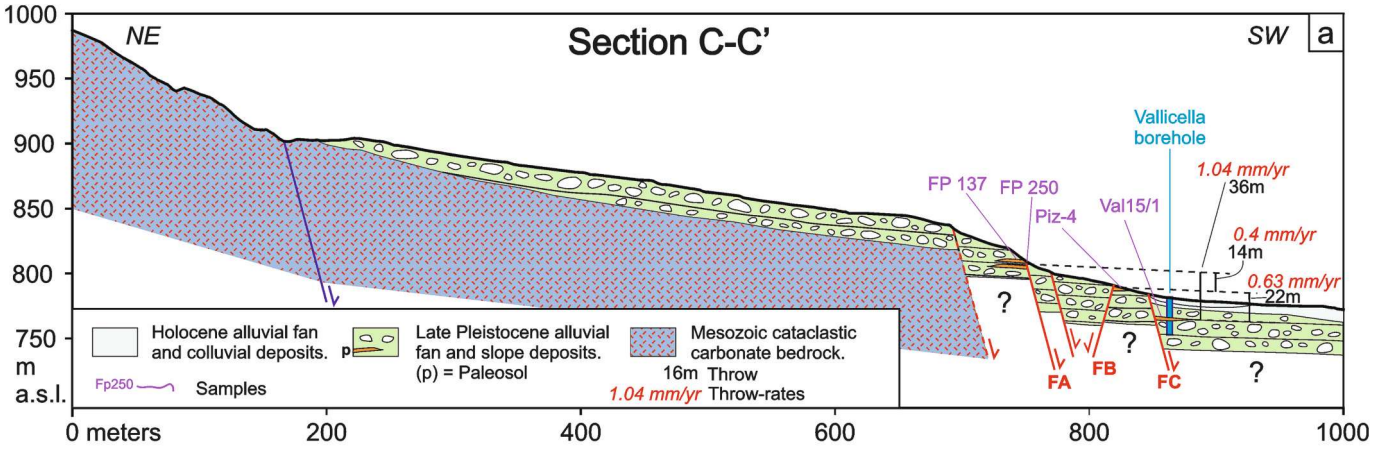

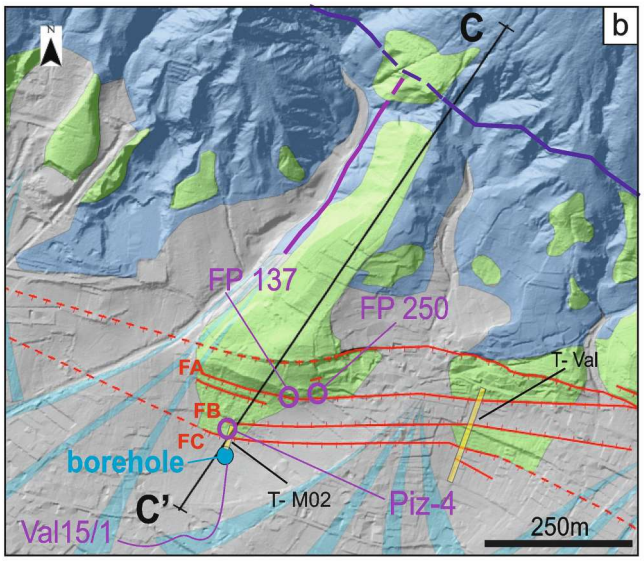

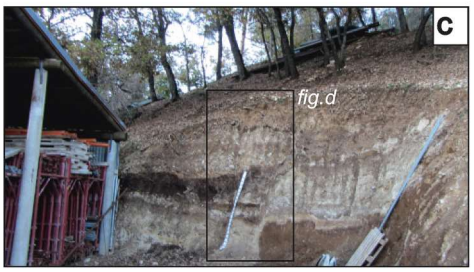

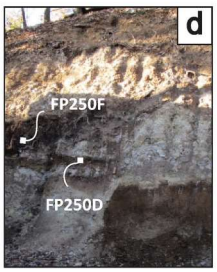

g) Radiocarbon ages of paleosols

Sample	Material	Measured Radioc. Age	2σ Calibration	References
PIZ4	organic sediment (paleosol)	30.310±310 BP	33286 – 32025 BC (34605 ± 630 BP)	Moro et al. 2002
VAL-15/1°	organic sediment (paleosol)	30.350±320 BP	33439 – 32316 BC (34827 ± 561 BP)	CARG sheet 348
FP250D*	charcoal (charred material)	35.700±700 BP	40002 – 37654 BC (40778 ± 1174 BP)	CARG sheet 348
FP250F*	organic sediment (paleosol)	34.441±400 BP	38673 – 36650 BC (39611 ±1011 BP)	CARG sheet 348
FP137*	organic sediment (paleosol)	24.974±75 BP	27369 – 27012 BC (29140 ± 178 BP)	CARG sheet 348

Fig. 8. Throw-rates of the Mt. Marine fault. A) Geological cross-section across the Vallicella area. This highlights the offset of dated paleosols embedded within the alluvial fan deposits, and the associated throw-rates of the main faults. B) Geological map showing the location of the cross-section trace, the dated paleosol and the borehole (legend in Fig. 2). C) Faulted paleosols in proximity of Fault A. D) Detailed photo of the faulted paleosols in C); it shows the location of the samples F250. E) Fault scarp associated with Fault A, where sample F137 was collected. F) Detailed photo of the paleosol sampled within the fault scarp of E). G) table of the radiocarbon ages collected along the cross-section C-C′. The ages are obtained from Moro et al. (2002) and by the CARG sheet 348, see therein for information on calibration.

the paleosol found in the borehole is 36 m. This offset converts into a combined throw-rate for Faults A and C of 1,04 mm/yr. The vertical offset between the same intermediate layer and Sample PIZ4 is 14 m, which converts in a throw-rate for Fault A of 0.4 mm/yr. The offset between Sample PIZ4 and VAL-15/1 is 22 m, which converts in a throw-rate for Fault C of 0.63 mm/yr. Hence, these results suggest that the Fault C hosts a larger throw-rate than Fault A over 35 kyrs.

Table 2
Summary of the throw-rates measurements obtained on the fault splays of the Mt. Marine fault.

Paleoseismological throw-rates of synthetic fault splays			
Fault	Minimum Throw (m)	Time interval of misuration (yrs)	Minimum Throw-rate (mm/yr)
FA	0.7	8000	0.3
FC	0.6	25,000	0.05
FD	0.45	15,000	0.08

Late Pleistocene throw-rates of syntethic fault splays (Vallicella area)			
Fault	Minimum Throw (m)	Time interval of misuration (yrs)	Throw-rate (mm/yr)
FA	14	35,000	0.4
FC	22	35,000	0.63
FA + FC	36	35,000	1.04

6. Discussion

The paleoseismological surveys performed across the Mt. Marine escarpment provide evidence of multiple Late Pleistocene-Holocene surface-rupturing seismic events on five synthetic and antithetic fault splays distributed within 500 m across strike. Our results suggest that most of the recent activity is localized on the synthetic splays, which have recorded more surface-rupturing events through time and larger coseismic throws, compared to the antithetic splays. In addition to that, we notice that the activity is not equally spread between the synthetic fault splays, as these recorded different earthquake rates through time: Fault A ruptured four times during the last 8 ka, Fault C recorded a very recent event (the 1703 CE) and two (or more) older surface-rupturing events (>20 ka), meanwhile Fault D experienced six surface-rupturing events during the last 22 ka.

The data we collected characterize the splays activity from unique locations of analysis. This practice could lead to misleading results, as evidence of paleoearthquakes may not be equally distributed along a fault (for instance, the formation and preservation of colluvial wedges and coseismic fault scarps may differ along the fault trace according to site-specific conditions, e.g., DuRoss et al., 2011). A common practice to constrain the slip history of an active fault is to integrate multiple data obtained from different sites of analysis along the same fault (e.g., Gómez-Novell et al., 2022). These data are then collated to reconstruct the activity of the overall fault. However, this approach would not allow us to discretize the specific activity of each fault splay composing the main fault. Hence, we treated each fault splay as a single fault, and reconstructed their slip histories by combining our paleoseismological results with published results of paleoseismological surveys performed on the Mt. Marine fault (Moro et al., 2002, 2016; Galli et al., 2011; Fig. 9). This approach allowed us to understand whether and how slip is localized across multiple fault splays of a zone of distributed deformation.

6.1. Slip localization across multiple fault splays

For each fault splay, we identified paleoearthquakes by comparing the slip histories obtained through our study and published data (Fig. 9). We defined paleoearthquakes as (i) simultaneous occurrence of surface-rupturing events on multiple sites along the same fault splay, and (ii) surface-rupturing events that have been found only on one site, even if the fault splay has been surveyed by multiple sites. That is because we must include the possibility that evidence of a paleoearthquake may have been preserved only in one site and may have been eroded in other sites. Given their structural arrangement of synthetic-antithetic faults and their across-strike proximity, we have considered Fault A-Fault B and Fault D-Fault E as pairs that are likely to rupture simultaneously during earthquakes. Hence, we have defined paleoearthquakes also by combining the slip histories of these two fault pairs (Fig. 9b.i and 9b.iii).

Fault A was observed in our Vallicella trench and in Trench B of Moro et al. (2016), meanwhile Fault B was observed in our Vallicella trench and in studies of Moro et al. (2002) and Galli et al. (2011) (Fig. 9b.i). In terms of identifying the most recent earthquake that ruptured Faults A and B, evidence of the 1703 CE earthquake was found on two out of five studies on Fault B (Galli et al.,2011, and Moro et al., 2002). Other surveys performed across Fault A (our Vallicella trench and Trench B of Moro et al., 2016) and Fault B (our Vallicella trench) show evidence of a recent earthquake for which there are none or poor constraints on its *ante quem* term. Keeping in mind that the most recent stratigraphic unit in the Vallicella trench is highly altered by anthropic activity, and considering that evidence of the most recent event of the 1703 CE were found in a trench located about 400 m to the west of the Vallicella trench (Fig. 9a), we infer that the 1703 earthquake may have ruptured Fault B, and consequently Fault A, also in the Vallicella trench, and that evidence of this have been elided by anthropic activity. Hence, we identify the 1703 CE earthquake as the most recent earthquake that ruptured the pair Fault A-Fault B (E1A). The penultimate paleoearthquake (E2A) is constrained by the event observed on Fault B in our Vallicella trench (ev1B). Assuming that Fault A and Fault B rupture simultaneously due to their structural arrangement, it follows that also Fault A in our Vallicella trench should have experienced such event. Therefore, Fault A experienced two events since 2000 BCE, and most likely the recent anthropic activity has elided evidence of one of them in the stratigraphic record of our Vallicella trench. Moreover, Galli et al. (2011) suggest the potential occurrence of an historical surface-rupturing event before 1600 CE (ev2B-G). Given the paleoseismological record observed on the other sites, we infer that this event could belong to E2A. As older data about Fault B are not available, older paleoearthquakes could be identified only on Fault A. The correlation of the events from our Vallicella trench and Trench B of Moro et al. (2016) allowed us to identify three older paleoearthquakes rupturing Fault A: E3A (3 ka BC-3.8 ka BC), E4A (3.8 ka BC-5 ka BC) and E5A (5 ka BC-6.1 ka BC).

Fault C has been observed in our Vallicella trench, in the trench of Moro et al. (2002) and in Trench A of Moro et al. (2016) (Fig. 9b.ii). All the three sites show evidence of a very recent event, which we can interpret to be representative of the 1703 CE earthquake. We therefore define the latter to be the most recent earthquake to rupture Fault C (E1C). As mentioned in Paragraph 4.2, although our Vallicella trench do not show a well constrained paleoseismological record between the 1703 CE and about 20 ka, the depth of CW suggests that other earthquakes may have occurred within this timeframe. Surveys of Moro et al. (2002, 2016) support this observation, as they highlight the occurrence of multiple events between 1703 CE and 20 ka. The cross-correlation of the two paleoseismological records allow us to discretize four more paleoearthquakes: E2C, occurred within 0–4 ka BC; E3C, occurred between 4 and 10 ka BC; E4C and E5C, occurred within 10–13 ka BC. The paleoseismological trenches of Moro et al. (2002, 2016) do not go further back in time, but our Vallicella trench reports the occurrence of

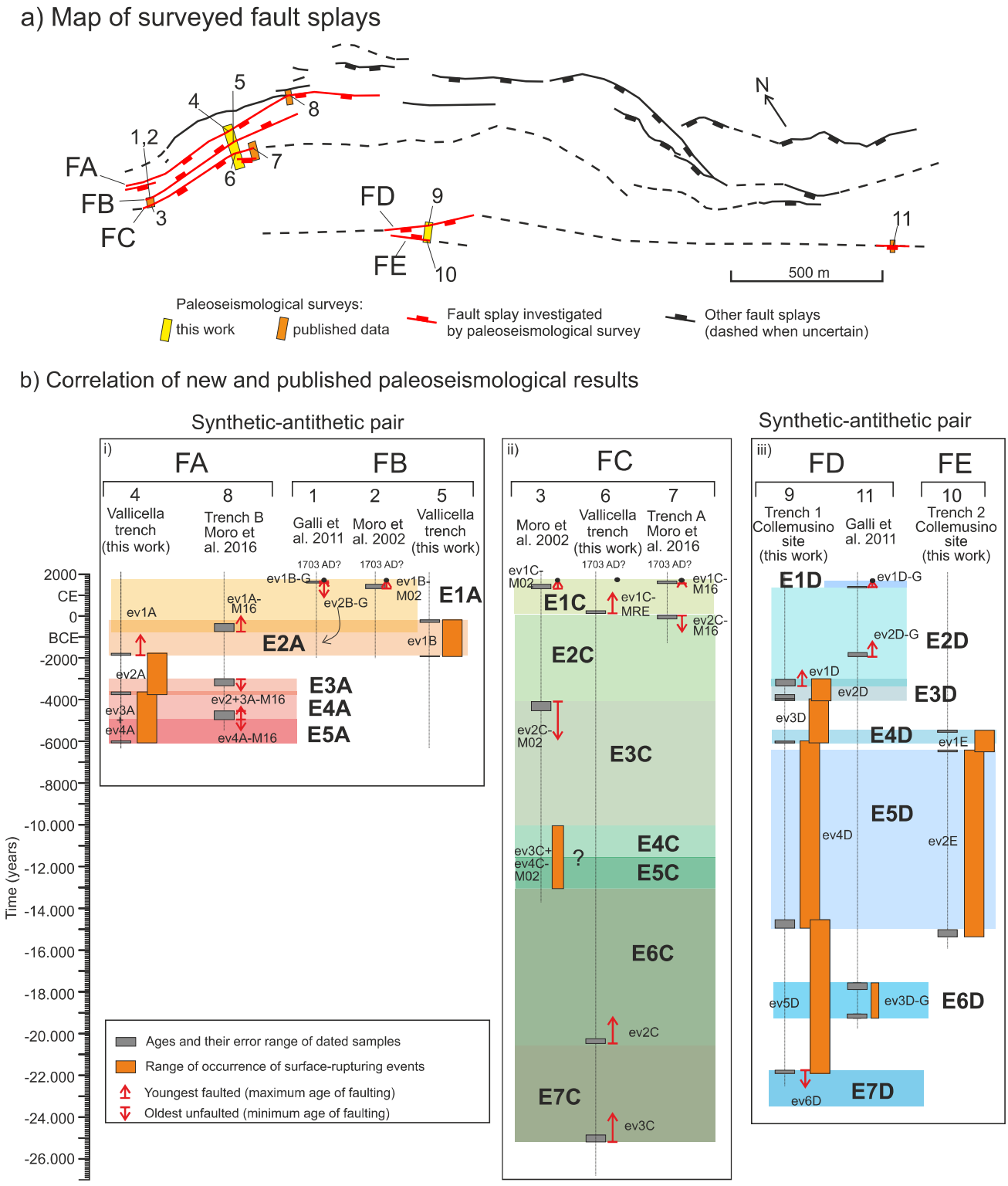

Fig. 9. Correlation between multiple paleoseismological surveys on the Mt. Marine fault. A) Map of the surveyed fault splays; in yellow are surveys presented in this study; in orange are surveys obtained from literature; numbers are referred to the specific fault analysis shown in b). B) Correlation of the new and published paleoseismological results. Each vertical line represents results from a specific study, the length of which indicates their time range of observation; these are grouped according to the fault splay they investigate. Grey boxes indicate the error bar in samples dates. Orange boxes are the range of occurrence of surface-rupture events on each splay. Red arrows indicate the range of occurrence of a surface-rupturing event in cases when only one of the *ante quem* or *post quem* terms are available; if the red arrow points upward, it means that the surface-rupturing event is younger than the age constraint from where the arrow begins; if the arrow points downward, the event is older than the age constraint. Shaded rectangular boxes are the interpreted correlation between multiple studies, which identifies paleoearthquakes on the specific splay (marked as E1A, E2A etc.). (For interpretation of the references to colour in this figure legend, the reader is referred to the web version of this article.)

two older earthquakes: E6C, younger than 20 ka BC, and E7C, dated 25.2 ka BC or younger.

Fault D has been investigated by our Trench 1 of the Collemusino site and Galli et al. (2011), meanwhile Fault E has been investigated only by our Trench 2 of the Collemusino site (Fig. 9b.iii). The combination of the paleoseismological records shows that Fault D experienced at least three earthquakes since 4000 BCE, with the most recent of them being the 1703 CE. E4D and E5D have been constrained by correlating our records on Fault D and Fault E, as Galli et al. (2011) presents a gap in the paleoseismological record. Specifically, E4D occurred between 5.5 and 6.1 ka BC, E5D occurred between 6.4 and 15 ka BC. We correlated an older event found by Galli et al. (2011) with our Trench 1 to constrain E6D between 15.6 ka BC and 19.3 ka BC. Finally, our Trench 1 provides evidence for an older earthquake, E7D, older than 21.8 ka BC.

The comparison between the different sites of analysis confirms our initial observation: the fault splays have recorded a different number of earthquakes through time. The pair Fault A-Fault B have recorded five earthquakes within the last 8 kyrs, Fault C has a continuous record of five earthquakes within the last 15 kyrs plus two older earthquakes, Fault D recorded six earthquakes within the last 26 kyrs. Hence, we suggest that fault linkage in the southern sector of the Mt. Marine fault is accommodated by slip partitioning between multiple synthetic and antithetic splay activated with different rates, with the activity appearing to be more intense on the inner fault splay (Fault A) at least for the last 8 ka.

6.2. Comparison between paleoseismological and Late-Pleistocene throw-rates

The paleoseismological surveys show that most of the activity over the last 8 ka is localized on Fault A, which hosted more earthquakes and has a larger throw-rate compared to the other fault splays. The 35 ka throw-rate of Fault C is larger than that of Fault A (Table 2). A potential uncertainty of the 35 ka throw-rate is due to the unknown exact depth time-horizon corresponding to 35 ka, which whether it has been eroded or lying within the clastic layers, it must remain between paleosols FP137 and FP250. If we consider the clastic layer dated 35 ka to be immediately above the 40 ka paleosol or underneath the 29 ka paleosol, we obtain a variability of throw-rate of about 0.1 mm/yr. This value lies within the uncertainty typically associated with throw-rate estimates from normal fault scarps (e,g., Faure Walker et al., 2021). If, on the other hand, there had been an erosional phase after 35 ka, we are confident that the thickness of the succession deposited between 40 ka and 35 ka must in any case be very thin, considering that the sedimentation in the footwall block is typically condensed compared to that of the hanging wall. Therefore, the uncertainty of the depth of the clastic layer dated 35 ka does not significantly influence our outcome.

Our results suggest that over 35 ka most of the slip was localized on Fault C, meanwhile slip localized on Fault A over the last 8 kyrs (Fig. 10a). This variability in throw-rates suggests that the locus of maximum activity swapped through time, with different splays accommodating most of the deformation in different time intervals. Hence, the activity over multiple fault splays appears to be clustered in space and time, with specific splays that take charge of most of the deformation in different time windows, which in this case was probably lasting for more than few tens of kyrs. The throw-rates we measured are consistent with published values for the same fault and in Central Apennines (e.g., Boncio et al., 2004; Roberts and Michetti, 2004; Carafa et al., 2022).

These findings of variable throw-rates of fault splays belonging to distributed faulting have implications on fault growth processes and in seismic hazard assessments. In terms of fault growth, our findings suggest that fault linkage across relay zones occurs through the localization of the activity on specific breaching faults through time. This means that, once multiple breaching faults are formed within a relay zone, only some of them will take charge of most of the deformation and develop in order to link the previously isolated fault segments.

In terms of seismic hazard, fault-based probabilistic assessments of both ground motion and fault displacement hazard are sensitive to slip-rate values (e.g., Coppersmith and Youngs, 2000). Whether the assessment is performed on a fault characterized by distributed deformation, slip-rate values derived by one fault splay may not accurately represent the slip-rate of the overall fault system, biasing the hazard assessment. Moreover, assigning uniformly a single value of slip-rate to multiple fault splays may cause an overestimation or underestimation of the actual likelihood of occurrence of the next surface displacement event for each fault splay. We suggest that, in case of distributed faulting, hazard assessments should be performed upon a careful analysis of the slip-rates of the multiple fault splays characterizing the fault in exam. The potential variation in space of the locus of maximum activity suggests that fault slip-rates should be measured over multiple time windows to obtain values that could better represent the fault behaviour.

6.3. Recurrence interval of large magnitude earthquakes on the Mt. Marine fault

In Section 6.1. we identified multiple earthquakes that have ruptured single splays. Although we have treated these splays as individual features, they are all connected at depth with the principal Mt. Marine fault. This means that we must consider that they may rupture simultaneously during large earthquakes, such as in the case of the Mw 6.7, 1703 CE earthquake (Fig. 9b). To identify large older earthquakes that have simultaneously ruptured multiple fault splays, we have compared the slip histories of each fault splay (Fig. 10b). We identified potential large earthquakes as the overlap of paleoearthquakes occurring on single splays associated with large coseismic slip. That is because large magnitude earthquakes would produce larger coseismic slip, and therefore it is likely that large earthquakes have caused large slip on multiple fault splays.

Following this principle, we hypothesize that there may have been two large older earthquakes, other than the 1703 CE. The first one potentially occurred between 3 ka BC and 3.4 ka BC. This is given by the contemporaneous occurrence of E3A, which produced a 60 cm-thick colluvial wedge on Fault A (ev2A, Fig. 4b-c), E2C and E3D, which caused a minimum of 20 cm of coseismic throw and ruptured multiple fault splays along Fault D (ev2D, Fig. 7a). An older potential large earthquake may have occurred between 5.5 ka BC and 6.1 ka BC, due to the overlap of E5A, which caused the formation of a 30 cm-thick colluvial wedge on Fault A (ev4A, Fig. 4b-c), E3C and E4D, which produced a 45 cm-thick colluvial wedge on Fault D (ev3D, Fig. 7a). We did not hypothesize large older earthquakes due to the lack of a paleoseismological record on the pair Fault A-Fault B.

If our analysis is correct, then we can envisage a behaviour of the Mt. Marine fault characterized by two different rupture scenarios (Fig. 10c): the fault releases lower magnitude earthquakes that cause surface rupture of specific fault splays with shorter recurrence interval, and larger magnitude earthquakes that rupture all the fault splays with longer recurrence interval (potentially 3–5 ka for the Mt. Marine fault). If we apply the Wells and Coppersmith (1994) Mw-maximum displacement (Dmax) scaling relationship to derive the magnitude of the two older potential large earthquakes from their largest measured coseismic slip, we obtain minimum magnitude of 6.3–6.4. We can infer these values as potential minimum thresholds for earthquakes rupturing simultaneously all the fault splays.

6.4. Implications from the comparison between measured coseismic throws and empirical scaling relationships

We have shown that each of the principal fault splays, Faults A, C and D, produced coseismic throws potentially up to 1.2 m, 0.9 m and 0.9 m, respectively. If we consider the entire length of the Mt. Marine fault (about 15 km from the Fault2SHA database, Faure Walker et al., 2021), the Dmax expected by the Dmax/surface rupture length (SRL) scaling

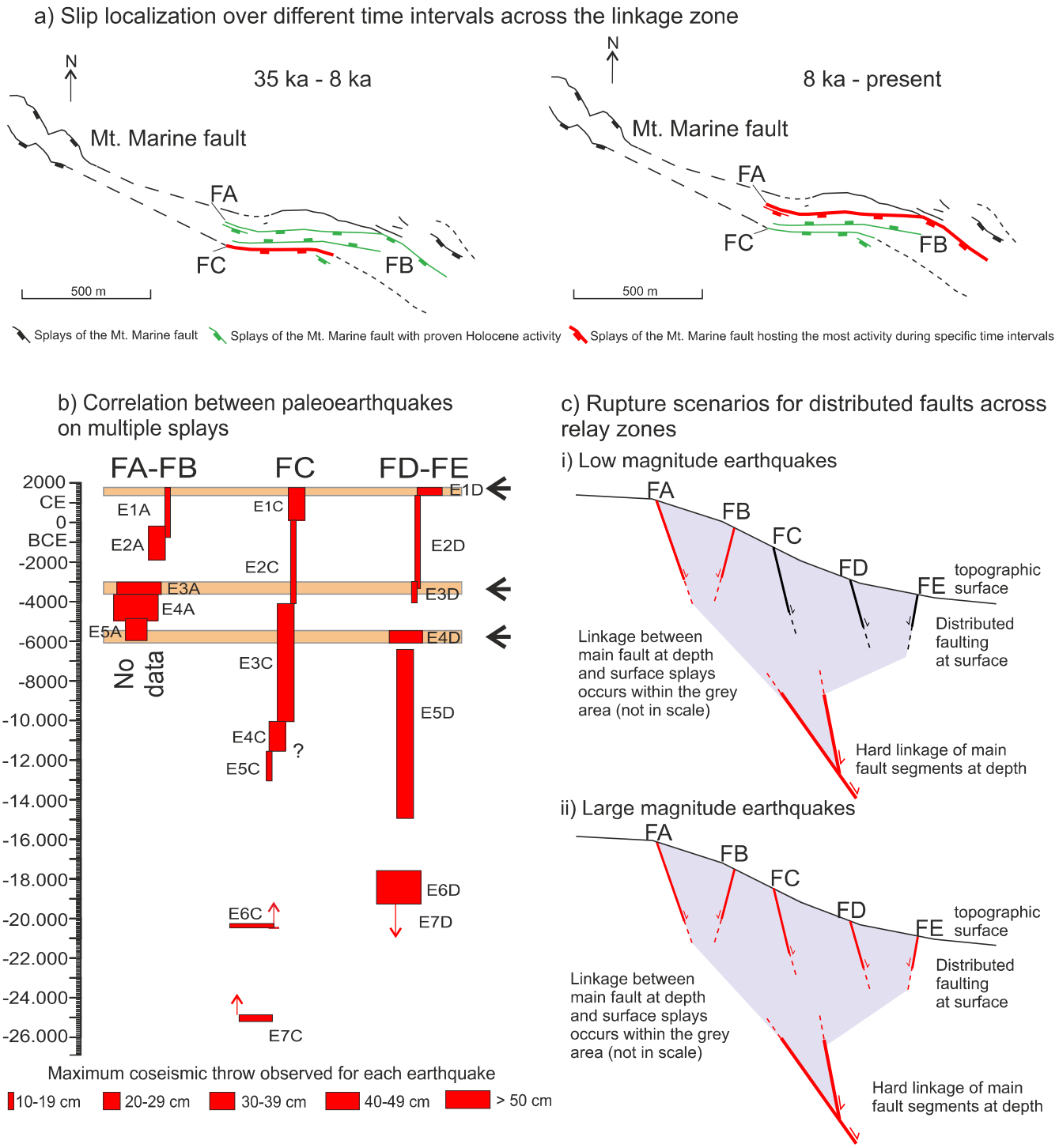

Fig. 10. Faulting dynamics over multiple splays. A) Slip localization over different time intervals across the fault bend in the Vallicella area. The figure shows how the activity was localized on Fault C during the time interval between 35 ka and 8 ka, and then moved on Fault A over the last 8 ka. B) Correlation between seismic histories of the multiple splays. In red are reported the paleoearthquakes identified on each splay; the thickness of the rectangles is function of the offset associated with the earthquakes. The shaded rectangular boxes mark the most likely combination of earthquakes that could indicate the occurrence of a large magnitude earthquake, which ruptured simultaneously multiple splays (indicated also with a black arrow). C) Conceptual model of rupture scenarios for distributed faults across the linkage zone. The grey area indicates the area interested by faulting associated with the Mt. Marine fault at depth and at the surface. The two sets are linked within the grey area, although we do not have enough information to envisage the structure of the linkage and its depth. In red are reported the surficial splays that rupture during earthquakes, in black those who do not rupture. This figure shows a conceptual model of distributed deformation on normal faults, in which low magnitude earthquakes rupture only specific fault splays, meanwhile large magnitude earthquakes rupture all the fault splays. (For interpretation of the references to colour in this figure legend, the reader is referred to the web version of this article.)

relationship of Wells and Coppersmith (1994) would be 0.7 m. Hence, the Dmax we observed in the field are larger than the expected Dmax. We acknowledge that these displacement values may include some post-seismic slip. Afterslip along the surface rupture up to 1.4 cm (throw), corresponding to ~10–15% of the maximum coseismic throw (10–15 cm), was measured by Wilkinson et al. (2012) after the 2009 Mw 6.3 L'Aquila earthquake using repeated terrestrial laser scan measurements. Centimeter-scale surface displacements interpreted as due to localized afterslip was detected after the Mw 6.52016 Norcia earthquake by Pousse-Beltran et al. (2020) using Interferometric Synthetic Aperture Radar time series. The modelled aftersip on the fault plane at the surface was $\leq$ of ~4 to 10 cm in the central part and southern termination of the main Mw 6.5 rupture (Fig. 8 in Pousse-Beltran et al., 2020). These values are only a very small percentage of the maximum displacement observed at the surface after the Mw 6.5 main shock (2.4 m; Civico et al., 2018). For the M. Marine fault, which is located in between the 2009 and 2016 earthquakes (Fig. 1), not having elements to discretize the coseismic and post-seismic slip components in a paleoseismological survey, we assume that eventual afterslip was negligible compared to the coseismic component. Recent papers have also suggested the possibility of aseismic deformation during the interseismic phase of an active fault on coherent carbonate rocks (e.g. Del Sole et al., 2023). Our study is focused on faults on incoherent and loose materials with multiple colluvial wedges that suggest that the dislocation occurs coseismically. Moreover, we have not identified any evidence of aseismic movement within the deposits and in the urban area in the surroundings. Hence, we assume that also eventual aseismic slip during interseismic phase is negligible. With these caveats, we propose two potential explanations for this.

Firstly, the survey is located within an overall along-strike fault bend, across which the fault splays have an oblique strike compared to the strike of the overall Mt. Marine fault (see Figs. 2 and 9a). Previous studies have suggested that the coseismic throw across a given location is controlled by the regional strain that the fault must accommodate and the local non-planar fault geometry (Faure Walker et al., 2009, 2010). It has been shown that coseismic throws tend to increase along fault bends in order to preserve the horizontal extensional rate along the fault and across the fault bend (Iezzi et al., 2018). Hence, one possible explanation for our large values of Dmax could be because the site was located within a fault bend, and therefore the coseismic throws are enhanced to preserve the horizontal strain along the fault. Considering the geological setting of the study area, the development of the fault bend along the Mt. Marine fault may be due to the presence of transversal Jurassic normal faults that could have acted as a segment boundary to the fault growth, resulting in a complex distribution of slip in space and time (e.g., Puliti et al., 2020; Fig. 2). In this scenario, the fault bend is growing to overcome this barrier, with the hard-linked fault at depth propagating upwards in an array of distributed splays that accommodate the deformation at surface (Fig. 10c).

Another potential explanation is provided by the interaction of the Mt. Marine fault with other nearby faults. Previous studies have in fact suggested that the Mt. Marine fault has the potential to rupture simultaneously with other faults of the Aterno Valley Fault System, generating larger magnitude earthquakes that will in turn produce larger coseismic throws at the surface (Blumetti and Guerrieri, 2007; Galli et al., 2011; Blumetti et al., 2013; Iezzi et al., 2019). For instance, Galli et al. (2011) identified paleoseismological evidence of the occurrence of the 1703 CE earthquake on multiple faults belonging to the Aterno Valley Fault System, suggesting that all these faults have ruptured simultaneously during such earthquakes. This suggests that the Mt. Marine fault has indeed the potential to release larger earthquakes than what expected given its geometry, and this would result in larger coseismic throws.

7. Conclusions

Our integrated geological-geomorphological-geophysical-paleoseismological work on the Mt. Marine normal fault (Abruzzo, Central Italy) provides insights on the dynamics of distributed faulting, showing that the single fault splays do not share the same history of activity, but they are active with differential slip-rates. We have shown that an overall fault bend in the southern sector of the Mt. Marine fault determines a large zone of distributed deformation accommodated by the activity of multiple synthetic and antithetic fault splays, all of which are able to release surface-rupturing earthquakes. The activity is localized in both space and time on specific fault splays. Potential large magnitude earthquakes, rupturing simultaneously multiple splays, seems to have large recurrence intervals (3–5 ka). Therefore, we suggest different scenarios in which (i) large magnitude earthquakes with long recurrence intervals rupture multiple fault splays, producing widespread distributed faulting; and (ii) smaller magnitude earthquakes, with shorter recurrence intervals rupturing single fault splays. This finding has important implications for seismic ground motion and fault displacement hazard assessments, as different slip-rates for multiple fault splays implies that in structurally complex faults with wide zones of distributed deformation distributed faults should not be treated as a whole, but each splay will include its own variables within hazard modelling.

CRediT authorship contribution statement

F. Iezzi: Writing – original draft, Visualization, Project administration, Methodology, Investigation, Formal analysis, Data curation, Conceptualization. **M. Francescone:** Writing – review & editing, Visualization, Methodology, Investigation, Data curation. **A. Pizzi:** Writing – review & editing, Validation, Supervision, Methodology, Investigation, Conceptualization. **A. Blumetti:** Writing – review & editing, Validation, Supervision, Methodology, Investigation, Conceptualization. **P. Boncio:** Writing – review & editing, Validation, Supervision, Methodology, Investigation, Funding acquisition, Conceptualization. **P. Di Manna:** Writing – review & editing, Validation, Methodology, Investigation. **B. Pace:** Writing – review & editing, Validation, Methodology, Investigation. **T. Piacentini:** Writing – review & editing, Validation, Methodology, Investigation. **F. Papasodaro:** Writing – review & editing, Validation, Methodology, Investigation. **F. Morelli:** Writing – review & editing, Visualization, Investigation. **M. Caciagli:** Writing – review & editing, Investigation. **M. Chiappini:** Writing – review & editing, Investigation. **F. D'Ajello Caracciolo:** Writing – review & editing, Investigation. **V. Materni:** Writing – review & editing, Investigation. **I. Nicolosi:** Writing – review & editing, Investigation. **V. Sapia:** Writing – review & editing, Investigation. **S. Urbini:** Writing – review & editing, Investigation.

Declaration of Competing Interest

The authors declare that they have no known competing financial interests or personal relationships that could have appeared to influence the work reported in this paper.

Data availability

All data are presented in figures, tables, and supplementary materials of this manuscript. Data from existing paleoseismological studies were collected from published papers (Moro et al., 2002, 2016; Galli et al., 2011; see their full reference in the References list). The DTM used in the figures is available at http://www.pcn.minambiente.it/mattm/. Historical earthquakes are available at https://emidius.mi.ingv.it/CPTI15-DBMI15_v3.0/. The geological map used as base for developing the one shown in Fig. 2 is available at https://www.isprambiente.gov.it/Media/carg/348_ANTRODOCO/Foglio.html. Existing databases and software mentioned in the main text are reported within the References List, marked with [Dataset] and [Software] and with the related DOI.

Acknowledgments

This work was realized under the agreement between the University of Chieti-Pescara (Dep. INGEO) and the National Institute of Geophysics and Vulcanology (INGV): "Ridefinizione delle Zone di Attenzione delle Faglie Attive e Capaci emerse dagli studi di microzonazione sismica effettuati nel territorio dei Centri abitati di Barete e Pizzoli in provincia de L'Aquila, interessati dagli eventi sismici verificatisi a far data dal 24 agosto 2016", funded by the Commissioner structure for post-earthquake reconstruction of the Italian Government. We thank Marco Moro, Stefano Gori and Emanuela Falcucci for their contributions in the early stages of the study. We thank the Editor Gideon Rosenbaum and two anonymous reviewers for the comments that helped us improving the manuscript.

Appendix A. Supplementary data

Supplementary data to this article can be found online at https://doi.org/10.1016/j.tecto.2023.230075.

References

Anderson, H., Jackson, J., 1987. Active tectonics of the Adriatic region. Geophys. J. Int. 91 (3), 937–983. https://doi.org/10.1111/j.1365-246X.1987.tb01675.

Beanland, S., Berryman, K.R., Blick, G.H., 1989. Geological investigations of the 1987 Edgecumbe earthquake, New Zealand. N. Z. J. Geol. Geophys. 32 (1), 73–91. https://doi.org/10.1080/00288306.1989.10421390.

Blumetti, A.M., 1995. Neotectonic investigations and evidence of paleoseismicity in the epicentral area of the January-February 1703, central Italy, earthquakes. In: Serva, L., Slemmons, B. (Eds.), Perspectives in Paleoseismology, 6. Ass. Engng. Geol., Spec. Publ, pp. 83–100.

Blumetti, A.M., Guerrieri, L., 2007. Fault-generated mountain fronts and the identification of fault segments: implications for seismic hazard assessment. Boll. Soc. Geol. Ital. 126 (2), 307.

Blumetti, A.M., Guerrieri, L., Vittori, E., 2013. The primary role of the Paganica-San Demetrio fault system in the seismic landscape of the Middle Aterno Valley basin (Central Apennines). Quat. Int. 288, 183–194. https://doi.org/10.1016/j.quaint.2012.04.040.

Boncio, P., Lavecchia, G., Pace, B., 2004. Defining a model of 3D seismogenic sources for Seismic Hazard Assessment applications: the case of central Apennines (Italy). J. Seismol. 8, 407–425. https://doi.org/10.1023/B:JOSE.0000038449.78801.05.

Bosi, C., Galadini, F., Giaccio, B., Messina, P., Sposato, A., 2003. Plio-Quaternary continental deposits in the Latium-Abruzzi Apennines: the correlation of geological events across different intermontane basins. Alpine Mediterranean Q. 16 (1 bis), 55–76.

Carafa, M.M.C., Di Naccio, D., Di Lorenzo, C., Kastelic, V., Bird, P., 2022. A Meta-Analysis of Fault Slip Rates Across the Central Apennines. J. Geophys. Res. Solid Earth 127 (1), e2021JB023252.

Caskey, S.J., Wesnousky, S.G., Zhang, P., Slemmons, D.B., 1996. Surface faulting of the 1954 Fairview Peak (MS 7.2) and Dixie Valley (MS 6.8) earthquakes, Central Nevada. Bull. Seismol. Soc. Am. 86 (3), 761–787. https://doi.org/10.1785/BSSA0860030761.

Cavinato, G.P., Celles, P.D., 1999. Extensional basins in the tectonically bimodal central Apennines fold-thrust belt, Italy: response to corner flow above a subducting slab in retrograde motion. Geology 27 (10), 955–958. https://doi.org/10.1130/0091-7613(1999)027<0955:EBITTB>2.3.CO;2.

Cinti, F.R., Pauselli, C., Livio, F., Ercoli, M., Brunori, C.A., Ferrario, M.F., Volpe, R., Civico, R., Pantosti, D., Pinzi, S., De Martini, P.M., Ventura, G., Alfonsi, L., Gambillara, R., Michetti, A.M., 2015. Integrating multidisciplinary, multiscale geological and geophysical data to image the Castrovillari fault (Northern Calabria, Italy). Geophys. J. Int. 203 (3), 1847–1863. https://doi.org/10.1093/gji/ggv404.

Cinti, F.R., Pantosti, D., Lombardi, A.M., Civico, R., 2021. Modeling of earthquake chronology from paleoseismic data: insights for regional earthquake recurrence and earthquake storms in the Central Apennines. Tectonophysics 816, 229016. https://doi.org/10.1016/j.tecto.2021.229016.

Civico, R., Pucci, S., Villani, F., Pizzimenti, L., De Martini, P.M., Nappi, R., Open EMERGEO Working Group, 2018. Surface ruptures following the 30 October 2016 M w 6.5 Norcia earthquake, Central Italy. J. Maps 14 (2), 151–160. https://doi.org/10.1080/17445647.2018.1441756.

Constable, S.C., Parker, R.L., Constable, C.G., 1987. Occam's inversion: a practical algorithm for generating smooth models from electromagnetic sounding data. Geophysics 52 (3), 289–300.

Coppersmith, K.J., Youngs, R.R., 2000. Data needs for probabilistic fault displacement hazard analysis. J. Geodyn. 29 (3–5), 329–343. https://doi.org/10.1016/S0264-3707(99)00047-2.

Cosentino, D., Asti, R., Nocentini, M., Gliozzi, E., Kotsakis, T., Mattei, M., Esu, D., Spadi, M., Tallini, M., Cifelli, F., Pennacchioni, M., Cavuoto, G., Di Fiore, V., 2017. New insights into the onset and evolution of the central Apennine extensional intermontane basins based on the tectonically active L'Aquila Basin (Central Italy). GSA Bull. 129 (9–10), 1314–1336.

Crone, A.J., Machette, M.N., Bonilla, M.G., Lienkaemper, J.J., Pierce, K.L., Scott, W.E., Bucknam, R.C., 1987. Surface faulting accompanying the Borah Peak earthquake and segmentation of the Lost River fault, central Idaho. Bull. Seismol. Soc. Am. 77 (3), 739–770.

D'Agostino, N., 2014. Complete seismic release of tectonic strain and earthquake recurrence in the Apennines (Italy). Geophys. Res. Lett. 41 (4), 1155–1162.

D'Agostino, N., Cheloni, D., Fornaro, G., Giuliani, R., Reale, D., 2012. Space-time distribution of afterslip following the 2009 L'Aquila earthquake. J. Geophys. Res. Solid Earth 117 (B2). https://doi.org/10.1029/2011JB008523.

DeGroot-Headlin, C., Constable, S.C., 1990. Occam's inversion to generate smooth, two dimensional models from magnetotelluric data. Geophysics 55, 1613–1624. https://doi.org/10.1190/1.1442813.

Del Sole, L., Mazzoli, S., Carafa, M.M.C., Toffol, G., Pennacchioni, G., Giuli, et al., 2023. Interseismic creep ofseismogenic carbonate-hosted normal faults: Insights from Central Italy. Geol. Soc. Am. Bull.

DePolo, C.M., Clark, D.G., Slemmons, D.B., Ramelli, A.R., 1991. Historical surface faulting in the Basin and Range province, western North America: implications for fault segmentation. J. Struct. Geol. 13 (2), 123–136. https://doi.org/10.1016/0191-8141(91)90061-M.

Devoti, R., d'Agostino, N., Serpelloni, E., Pietrantonio, G., Riguzzi, F., Avallone, A., et al., 2017. A combined velocity field of the Mediterranean region. Ann. Geophys. 60.

Doglioni, C., 1991. A proposal for the kinematic modelling of W-dipping subductions-possible applications to the Tyrrhenian-Apennines system. Terra Nova 3 (4), 423–434. https://doi.org/10.1111/j.1365-3121.1991.tb00172.x.

DuRoss, C.B., Personius, S.F., Crone, A.J., Olig, S.S., Lund, W.R., 2011. Integration of paleoseismic data from multiple sites to develop an objective earthquake chronology: application to the Weber segment of the Wasatch fault zone, Utah. Bull. Seismol. Soc. Am. 101 (6), 2765–2781. https://doi.org/10.1785/0120110102.

Faure Walker, J., Roberts, G.P., Cowie, P.A., Papanikolaou, I.D., Sammonds, P.R., Michetti, A.M., Phillips, R.J., 2009. Horizontal strain-rates and throw-rates across breached relay zones, Central Italy: implications for the preservation of throw deficits at points of normal fault linkage. J. Struct. Geol. 31 (10), 1145–1160. https://doi.org/10.1016/j.jsg.2009.06.011.

Faure Walker, J.P., Roberts, G.P., Sammonds, P.R., Cowie, P., 2010. Comparison of earthquake strains over 10^2 and 10^4 year timescales: insights into variability in the seismic cycle in the central Apennines, Italy. J. Geophys. Res. Solid Earth 115 (B10). https://doi.org/10.1029/2009JB006462.

Faure Walker, J., Roberts, G.P., Cowie, P.A., Papanikolaou, I., Michetti, A.M., Sammonds, P., Wilkinson, M., McCaffrey, K.J.W., Phillips, R.J., 2012. Relationship between topography, rates of extension and mantle dynamics in the actively-extending Italian Apennines. Earth Planet. Sci. Lett. 325, 76–84. https://doi.org/10.1016/j.epsl.2012.01.028.

Faure Walker, J., Boncio, P., Pace, B., Roberts, G., Benedetti, L., Scotti, O., et al., 2021. Fault2SHA Central Apennines database and structuring active fault data for seismic hazard assessment. [Dataset]. Sci. Data 8 (1), 1–20. https://doi.org/10.1038/s41597-021-00868-0.

Galadini, F., Galli, P., 2000. Active tectonics in the central Apennines (Italy)-input data for seismic hazard assessment. Nat. Hazards 22 (3), 225. https://doi.org/10.1023/A:1008149531980.

Galli, P., Galadini, F., Pantosti, D., 2008. Twenty years of paleoseismology in Italy. Earth Sci. Rev. 88 (1–2), 89–117. https://doi.org/10.1016/j.earscirev.2008.01.001.

Galli, P.A., Giaccio, B., Messina, P., Peronace, E., Zuppi, G.M., 2011. Palaeoseismology of the L'Aquila faults (Central Italy, 2009, M w 6.3 earthquake): implications for active fault linkage. Geophys. J. Int. 187 (3), 1119–1134. https://doi.org/10.1111/j.1365-246X.2011.05233.x.

Gómez-Novell, O., Ortuño, M., García-Mayordomo, J., Insua-Arévalo, J.M., Rockwell, T. K., Baize, S., et al., 2022. Improved geological slip rate estimations in the complex Alhama de Murcia Fault zone (SE Iberia) and its implications for fault behavior. Tectonics 41 (12). https://doi.org/10.1029/2022TC007465 e2022TC007465.

Iezzi, F., Mildon, Z., Walker, J.F., Roberts, G., Goodall, H., Wilkinson, M., Robertson, J., 2018. Coseismic throw variation across along-strike bends on active normal faults: implications for displacement versus length scaling of earthquake ruptures. J. Geophys. Res. Solid Earth 123 (11), 9817–9841. https://doi.org/10.1029/2018JB016732.

Iezzi, F., Roberts, G., Walker, J.F., Papanikolaou, I., 2019. Occurrence of partial and total coseismic ruptures of segmented normal fault systems: insights from the Central Apennines, Italy. J. Struct. Geol. 126, 83–99. https://doi.org/10.1016/j.jsg.2019.05.003.

Lavecchia, G., Brozzetti, F., Barchi, M., Menichetti, M., Keller, J.V., 1994. Seismotectonic zoning in east-Central Italy deduced from an analysis of the Neogene to present deformations and related stress fields. GSA Bull. 106 (9), 1107–1120. https://doi.org/10.1130/0016-7606(1994)106<1107:SZIECI>2.3.CO;2.

Livio, F., Michetti, A.M., Vittori, E., Gregory, L., Wedmore, L., Piccardi, L., Central Italy Earthquake Working, 2016. Surface faulting during the August 24, 2016, Central Italy earthquake (Mw 6.0): preliminary results. Ann. Geophys. 59 (5), 1–8. https://doi.org/10.4401/ag-7197.

Loke, M.H., 2012. Tutorial: 2-D and 3-D Electrical Imaging Surveys. [Software]. Geotomo Software, Malaysia.

Mansfield, C., Cartwright, J., 2001. Fault growth by linkage: observations and implications from analogue models. J. Struct. Geol. 23 (5), 745–763. https://doi.org/10.1016/S0191-8141(00)00134-6.

McCalpin, J., Ferrario, F., Figueiredo, P., Livio, F., Grützner, C., Pisarska-Jamroży, M., et al., 2023. New developments in onshore paleoseismic methods, and their impact

on Quaternary tectonic studies. Quat. Int. 664, 59–76. https://doi.org/10.1016/j.quaint.2023.03.008, 10 August 2023.
Messina, P., Moro, M., Speranza, F., 2001. Primi risultati di stratigrafia magnetica su alcune formazioni continentali dell'alta valle dell'Aterno (Italia centrale). Il Quaternario 14, 167–172.
Milliner, C.W., Dolan, J.F., Hollingsworth, J., Leprince, S., Ayoub, F., Sammis, C.G., 2015. Quantifying near-field and off-fault deformation patterns of the 1992 Mw 7.3 L anders earthquake. Geochem. Geophys. Geosyst. 16 (5), 1577–1598. https://doi.org/10.1002/2014GC005693.
Morelli, G., Labrecque, D.J., 1996. Advances in ERT inverse modelling. Eur. J. Environ. Eng. Geophys. 1, 171–186.
Moro, M., Bosi, V., Galadini, F., Galli, P., Giaccio, B., Messina, P., Sposato, A., 2002. Analisi paleosismologiche lungo la faglia del M. Marine (alta valle dell'Aterno): risultati preliminari. Il Quaternario 15, 267–278.
Moro, M., Falcucci, E., Gori, S., Saroli, M., Galadini, F., 2016. New paleoseismic data across the Mt. Marine Fault between the 2016 Amatrice and 2009 L'Aquila seismic sequences (central Apennines). In: Annals of Geophisycs, Fast Track 5/ 59. https://doi.org/10.4401/ag-7260.
Nurminen, F., Baize, S., Boncio, P., Blumetti, A.M., Cinti, F.R., Civico, R., Guerrieri, L., 2022. SURE 2.0–New release of the worldwide database of surface ruptures for fault displacement hazard analyses. [Dataset]. Sci. Data 9 (1), 729. https://doi.org/10.1038/s41597-022-01835-z.
Pace, B., Visini, F., Peruzza, L., 2016. FiSH: MATLAB tools to turn fault data into seismic-hazard models. Seismol. Res. Lett. 87 (2A), 374–386. https://doi.org/10.1785/0220150189.
Papanikolaou, I.D., Roberts, G.P., Michetti, A.M., 2005. Fault scarps and deformation rates in Lazio–Abruzzo, Central Italy: comparison between geological fault slip-rate and GPS data. Tectonophysics 408 (1–4), 147–176. https://doi.org/10.1016/j.tecto.2005.05.043.
Piacentini, T., Miccadei, E., 2014. The role of drainage systems and intermontane basins in the Quaternary landscape of the Central Apennines chain (Italy). Rendiconti Lincei 25, 139–150.
Pizzi, A., Galadini, F., 2009. Pre-existing cross-structures and active fault segmentation in the northern-central Apennines (Italy). Tectonophysics 476 (1–2), 304–319. https://doi.org/10.1016/j.tecto.2009.03.018.
Pizzi, A., Scisciani, V., 2000. Methods for determining the Pleistocene–Holocene component of displacement on active faults reactivating pre-Quaternary structures: examples from the central Apennines (Italy). J. Geodyn. 29 (3–5), 445–457. https://doi.org/10.1016/S0264-3707(99)00053-8.
Pousse-Beltran, L., Socquet, A., Benedetti, L., Doin, M.-P., Rizza, M., D'Agostino, N., 2020. Localized afterslip at geometrical complexities revealed by InSAR after the 2016 Central Italy seismic sequence. J. Geophys. Res. Solid Earth 125. https://doi.org/10.1029/2019JB019065 e2019JB019065.
Puliti, I., Pizzi, A., Benedetti, L., Di Domenica, A., Fleury, J., 2020. Comparing slip distribution of an active fault system at various timescales: Insights for the evolution of the Mt. Vettore-Mt. Bove fault system in Central Apennines. Tectonics 39. https://doi.org/10.1029/2020TC006200 e2020TC006200.
Roberts, G.P., Michetti, A.M., 2004. Spatial and temporal variations in growth rates along active normal fault systems: an example from the Lazio-Abruzzo Apennines, Central Italy. J. Struct. Geol. 26 (2), 339–376. https://doi.org/10.1016/S0191-8141(03)00103-2.
Roberts, G.P., Raithatha, B., Sileo, G., Pizzi, A., Pucci, S., Walker, J.F., et al., 2010. Shallow subsurface structure of the 2009 April 6 M w 6.3 L'Aquila earthquake surface rupture at Paganica, investigated with ground-penetrating radar. Geophys. J. Int. 183 (2), 774–790. https://doi.org/10.1111/j.1365-246X.2010.04713.x.
Rovida, A., Locati, M., Camassi, R., Lolli, B., Gasperini, P., 2020. The Italian earthquake catalogue CPTI15. Bull. Earthq. Eng. 18 (7), 2953–2984. https://doi.org/10.1007/s10518-020-00818-y.
Rovida, A., Locati, M., Camassi, R., Lolli, B., Gasperini, P., Antonucci, A., 2022. Catalogo Parametrico dei Terremoti Italiani (CPTI15), versione 4.0. [Dataset] Istituto Nazionale di Geofisica e Vulcanologia (INGV). https://doi.org/10.13127/CPTI/CPTI15.4.
Sarmiento, A., Madugo, D., Bozorgnia, Y., Shen, A., Mazzoni, S., Lavrentiadis, G., Dawson, T., Madugo, C., Kottke, A., Thompson, S., Baize, S., Milliner, C., Nurminen, F., Boncio, P., Visini, F., 2021. Report GIRS 2021–08: Fault Displacement Hazard Initiative Database. [Dataset]. https://doi.org/10.34948/N36P48.
Servizio Geologico d''Italia, 2022. Carta Geologica d'Italia alla scala 1:50,000, F. 348 Antrodoco. ISPRA, Roma. https://doi.org/10.15161/oar.it/75554.
Suter, M., 2015. Rupture of the Pitáycachi Fault in the 1887 Mw 7.5 Sonora, Mexico earthquake (southern Basin-and-Range Province): rupture kinematics and epicenter inferred from rupture branching patterns. J. Geophys. Res. Solid Earth 120, 617–641. https://doi.org/10.1002/2014JB011244.
Teran, O.J., Fletcher, J.M., Oskin, M.E., Rockwell, T.K., Hudnut, K.W., Spelz, R.M., et al., 2015. Geologic and structural controls on rupture zone fabric: a field-based study of the 2010 Mw 7.2 El Mayor–Cucapah earthquake surface rupture. Geosphere 11 (3), 899–920. https://doi.org/10.1130/GES01078.1.
Testa, A., Valentini, A., Boncio, P., Pace, B., Visini, F., Mirabella, F., Pauselli, C., 2021. Probabilistic fault displacement hazard analysis of the Anghiari–Città di Castello normal fault (Italy). Ital. J. Geosci. 140 (3), 327–346. https://doi.org/10.3301/IJG.2021.07.
Valentini, A., Visini, F., Pace, B., 2017. Integrating faults and past earthquakes into a probabilistic seismic hazard model for peninsular Italy. Nat. Hazards Earth Syst. Sci. 17 (11) https://doi.org/10.5194/nhess-17-2017-2017.
Visini, F., Valentini, A., Chartier, T., Scotti, O., Pace, B., 2020. Computational tools for relaxing the fault segmentation in probabilistic seismic hazard modelling in complex fault systems. Pure Appl. Geophys. 177, 1855–1877. https://doi.org/10.1007/s00024-019-02114-6.
Walsh, J.J., Bailey, W.R., Childs, C., Nicol, A., Bonson, C.G., 2003. Formation of segmented normal faults: a 3-D perspective. J. Struct. Geol. 25 (8), 1251–1262. https://doi.org/10.1016/S0191-8141(02)00054-8.
Wells, D.L., Coppersmith, K.J., 1994. New empirical relationships among magnitude, rupture length, rupture width, rupture area, and surface displacement. Bull. Seismol. Soc. Am. 84 (4), 974–1002. https://doi.org/10.1785/BSSA0840040974.
Wilkinson, M.W., McCaffrey, K.J.W., Roberts, G.P., Cowie, P.A., Phillips, R.J., Degasperi, M., et al., 2012. Distribution and magnitude of post-seismic deformation of the 2009 L′ Aquila earthquake (M 6.3) surface rupture measured using repeat terrestrial laser scanning. Geophys. J. Int. 189 (2), 911–922. https://doi.org/10.1111/j.1365-246X.2012.05418.x.
Youngs, R.R., Arabasz, W.J., Anderson, R.E., Ramelli, A.R., Ake, J.P., Slemmons, D.B., et al., 2003. A methodology for probabilistic fault displacement hazard analysis (PFDHA). Earthquake Spectra 19 (1), 191–219. https://doi.org/10.1193/1.1542891.